RESEARCH

Open Access

Numerical and Experimental Behavior of Two-Story Confined Masonry Structure Subjected to Cyclic Loads

Mosaad El-Diasity[1], Sayed Salah[1], Mohamed O. R. El-Hariri[1], Amr A. Gamal[1] and Tarik S. Elsalakawy[1*]

Abstract

This research presents the numerical and experimental results of lateral cyclic loading applied on a two-story confined masonry structure utilizing local materials and standards. Two half-scale confined masonry structures were constructed using clay masonry units, confining columns, tie beams, and reinforced concrete slabs. The assemblies were tested up to failure using a displacement controlled loading methodology under vertical self-weight and lateral reversed cyclic loading. The walls of the assemblies have varying perforations (solid / windows / doors) to examine the influence of perforation on in-plane and out-of-plane performance. A strengthened assembly with an exterior layer of ferrocement has been used and this suggested upgrading approach enhanced the lateral resistance of the confined assembly by about (61–95%) while improving ductility and total energy absorbed by 27%. The maximum lateral drift at failure have been decreased to (23–31%), however the corresponding load for the first visible fracture have been raised by (150–175%). Furthermore, total failure has been delayed for the strengthened walls (all sides, particularly the perforated sides). Comparing distorted forms, fracture patterns, and capacity curves of finite element models included in this research yielded excellent agreement.

Keywords Masonry building, Confined masonry, Seismic behavior, Cyclic loading, Shear failure, Ferrocement

1 Introduction

A correctly designed confined masonry system enhances both deformation and energy dissipation properties over an unreinforced masonry system (Tomazevic & Klemence, 1997). Different researches study the confinement of brick walls to enhance the vertical and seismic behavior using ferrocement and the results in terms of ultimate loads, displacement and energy dissipation shows that the system can effectively increase the ultimate capacity as well as the deformation and energy dissipation of the studied samples (Ashraf et al., 2012; Chourasia et al., 2019; Gupta & Singhal, 2020).

El-Diasity and others, investigated the performance of in-plane confined masonry walls strengthened with ferrocement and GFRP systems and the experimental results reveals the enhancement of the ultimate failure loads of the specimen with considerable rise in ductility and energy absorption accompanied with less improvement in lateral drifts (El-Diasity et al., 2015; ElGawady et al., 2005; Yu et al., 2007).

The toothed connection between the RC columns used for the confinement and the masonry walls increase the ability of this type of connection to enhance the load capacity of confined masonry walls when subjected to lateral loads and provide more ductility. This composite action is gained by the interlocking between the walls and the tie columns. In the absence of toothing, composite

*Correspondence:
Tarik S. Elsalakawy
tarek.abdelgalil@feng.bu.edu.eg
[1] Structural Engineering Department, Shoubra Faculty of Engineering,
Benha University, Benha, Egypt

El-Diasity *et al. Int J Concr Struct Mater* (2023) 17:70

Page 2 of 30

action can be achieved through reinforcement (horizontal dowels) (Yacila et al., 2019).

Perez et al., (2009) and Choayb et al., (2021) investigated a two-bay CM specimen exposed to reversed cyclic lateral loading to simulate earthquake impacts. The specimen exhibits a common damage pattern in the form of diagonal shear cracks. The breakdown manifested itself as a conspicuous diagonal fracture that progressed through the walls and tie columns.

The size of the opening and the coupling between the two walls around the opening (in terms of concrete dimensions and steel reinforcement) influence both the initial stiffness and the cracking pattern (Ishibashi et al., 1992). While overly large apertures may impair the shear capacity of confined masonry walls by almost 50% (Gostic & Zarnic, 1999), their influence on seismic performance is essentially minimal when size is limited to 10% of the wall gross area (Yanez et al., 2004).

The confinement given on both sides of windows/doors indicates the necessity of confinement all around the openings for good seismic performance in terms of overall better behavior due to more distributed damage and greater ductility (Singhal & Rai, 2018). It is well acknowledged that adding reinforcement around door opening enhances the behavior of masonry walls. Flores et al., (2004) examined two restrained walls under cyclic loads and found that tie columns/beams around apertures minimize corner damage and enhance deformation capacity. Kuroki et al., (2012) examined five specimens with window opening and four with door openings under cyclic lateral loads with varying opening locations and confinement. The key finding was that specimens with reinforcing concrete components on the opening perimeter could acquire greater load capacity.

Flores and Alcocer (1996) and El-Salakawy and Hamdy (2021) create a mathematical model to characterize the non-linear behavior of confined masonry constructions constructed with hand-made clay bricks. The model's recommended envelope curve is a tri-linear force–deformation curve generated from material parameters and wall geometry. Yoshimura et al., (2004)) also developed an experimental study on the effects of lateral force, column and wall reinforcements on seismic behavior of confined masonry to study the ultimate shear strengths of confined masonry wall constructed using concrete hollow block units.

The modeling of the interface between brick units and mortar bed joints has been divided into two categories, the first of which assumes that the bricks and mortar are fully integrated and that the element nodes on the contact surface satisfy the criteria for continuous displacement. Therefore, the degrees of freedom on

the connected elements of the contact surface are coupled. The other method takes into account bond–slip between brick units and mortar bed joints, necessitating the implementation of an interface element (Tarek et al., 2020; Yan et al., 2011). Using the "ANSYS® (ANSYS® Academic Research, Release 12.0)" solid65 element, they investigated the characteristics and qualities of masonry and computationally modeled the shear properties of joints in masonry structures subject to varying vertical loads (fm). Upon comparing the experimental and numerical results, the recommended values for the shear transfer coefficient for the Solid65 element for modeling of masonry structures were determined to be 0.3 to 0.6 (Sandeep et al., 2013; Tarek et al., 2020).

As part of a research effort aimed at producing structurally and economically effective hybrid building systems for developing nations in general, and Egypt specifically. This research studies the lateral load behavior of a strengthened constrained masonry 3D-building constructed with a low-cost ferrocement system planned and manufactured using locally accessible materials and conventional craftsmanship and construction practices.

2 Experimental Program

The experimental program investigates the in-plane and out-of-plane performance of a ferrocement-strengthened CM (confined masonry) building using expanded mesh as an externally bonded upgrade material that is low-cost retrofitting techniques. Both strengthened and non-strengthened CM building will be tested to failure under cyclic loads.

2.1 The Tested Assemblies' Description

Two half-scale confined masonry 3D structures have been constructed, the test samples are made up of clay masonry units, tie columns, tie beams, and R.C. slabs. The assemblies were tested up to failure using a displacement controlled loading protocol under vertical self-weight and lateral reversed cyclic loading. The walls of the assemblies have varying perforations (solid / windows / doors) to investigate the effect of perforation on in-plane and out-of-plane performance. A strengthened assembly with an exterior layer of ferrocement is also available. The CM structure is two stories building with in plan dimensions of 1.50×1.50 m and a total height of 2.60 m. Each level's R.C. slab thickness is 100 mm, with reinforcing mesh T10@200, the masonry wall thickness is 100 mm. Each level's wall layout is as follows: two solid walls, one perforated with a window opening of 0.34×0.34 m and the other with a door opening of 0.36×0.64 m, as demonstrated in the typical four perspectives as shown in Figs. 1 and 2. The tested assemblies
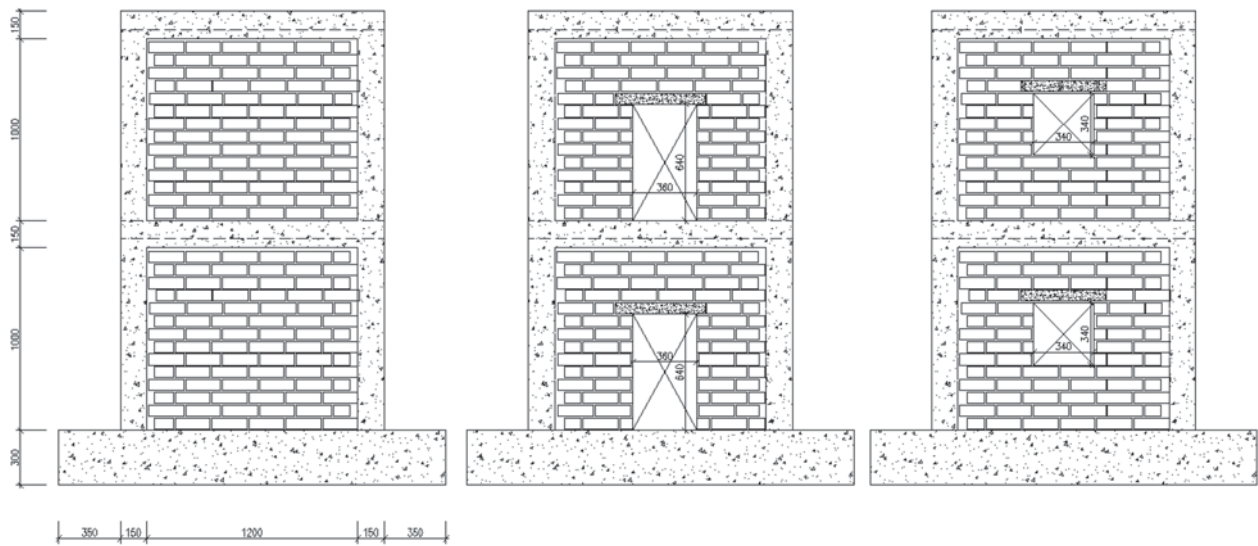
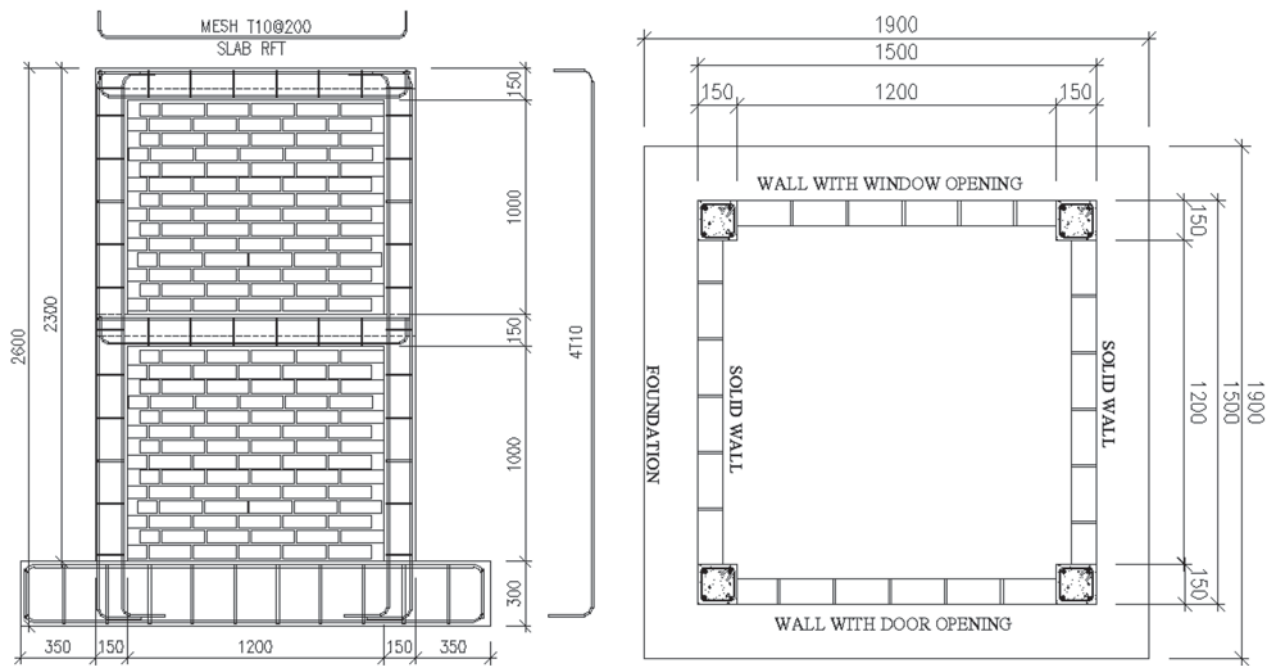**Fig. 1** Elevations for the solid/perforated walls

Fig. 2 Typical RFT detail (elevation), typical plan layout

Table 1 Summary of tested 3D assemblies' design

Assembly ID	Upgrading state	Tie column dim		Tie beam dim		Long RFT	Trans RFT
		B (mm)	L (mm)	B (mm)	L (mm)		
S-01	Un-strengthened	150	150	150	150	4T10	T6@20 cm
S-02	Strengthened	150	150	150	150	4T10	T6@20 cm

are summarized in Table 1. The retrofitting assembly was developed using full covering of the exterior face of all walls with ferrocement wire mesh, fixed to the walls using shear connectors. Fig. 3 depicts the building of wall assemblies and Fig. 4 shows the retrofitting steps.

The 3D assembly (S-02) was strengthened with one ferrocement layer made of wire mesh with thickness 1.6 mm and grid size of 15×35 mm. The mesh grade is 240/350 with a yield stress (fy) of 240 MPa, ultimate tensile strength (fu) of 350 MPa, and elastic modulus (Es) of 200 GPa. The enlarged mesh was attached to the masonry wall by nailing it every 100 mm in both directions and

then coating it with a 20-mm-thick mortar, as indicated in Fig. 4. The mortar properties type 1 content of cement and sand with volumetric ratio of 1:3, respectively, and a w/c ratio of 0.5, the mortar compressive strength f'm after 28 days was 20.5 MPa.

Concrete compressive strength (Fcu) for the concrete columns, slabs and ties has been determined using standard cube compression test and the average compressive strength determined to be 24.5 MPa, also the average masonry prisms compressive strength (f'm) was 4.8 MPa

(a) Base footing and columns dowels

(b) construction of level 1 masonry walls

(c) Casting of R.C. columns/beams/slab of 1st level

(d) the last instance of an un- strengthened assembly (S-01)

Fig. 3 A typical 3D assembly's construction sequence

(a) Wall splatter-dashing   (b) Fixing the ferrocement Mesh   (c) Applied mortar layer

Fig. 4 Ferrocement's retrofitting 3D assembly procedures

(ASTM E519-02, 2002). The main reinforcement for concrete element has been developed using high strength steel with yield and ultimate strength of 360/520 MPa, while the transverse reinforcement was mild steel bars with yield and ultimate strength of 240/350 MPa. The walls have been cured for 28 days before testing and painted with white paint to help record the failure cracks. Three masonry wallets (800×800×100 mm) were constructed and subjected to a diagonal compression test in accordance with ASTM E519-02 (ASTM E519-02, 2002) to assess diagonal tensile strength as shown in Fig. 5, the average tensile stress f_t for wallet specimens equals 0.78 MPa according to equations and expressions of Eurocode 6 (Committee & for Standardisation, 1995) and Eq. 1, the RILEM committee (RILEM TC, 1994) and (Garcı et al., 2019):

$$q0 = ft = \frac{0.707 Pult}{An}, \qquad (1)$$

where P ult is the maximum load that it supports in wallet, and An is the net cross section of the wallet.

2.2 Test Configuration

The 3D assemblies were evaluated under vertical self-weight and lateral reversed cyclic loading using a
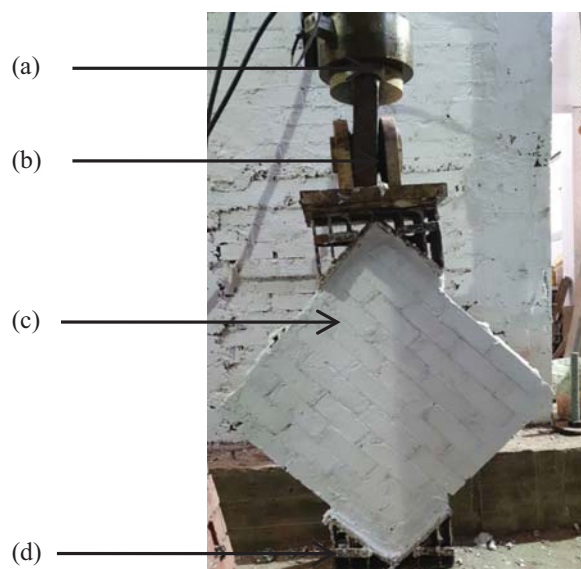
Fig. 5 Test set up of diagonal compression test, **a** hydraulic jack; **b** load cell; **c** loading shoes; **d** masonry specimen

Fig. 6 Test configuration
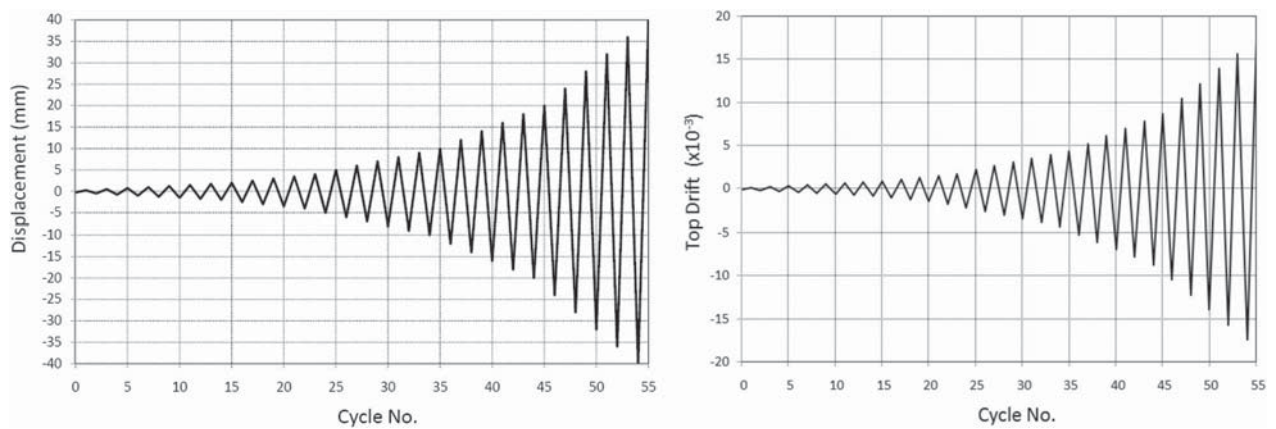
Fig. 7 Protocol for cyclic displacement and drift

El-Diasity *et al. Int J Concr Struct Mater*   (2023) 17:70

Page 7 of 30

displacement controlled loading methodology until failure, as shown in Fig. 6. In this regard, a steel beam was inserted between the jack plate and the final surface of the specimen to allow consistent loading at the top level without localized fracture of the building. A 600-kN hydraulic actuator was used to provide the lateral cyclic load. The horizontal loading is provided to the wall through controlled displacement protocol at a rate of 60 m/s, as illustrated in Fig. 7. The foundation was anchored to the reaction floor by six bolts (32 mm) spaced 80 cm apart to avoid overturning and sliding during testing. At the conclusion of each cycle, the displacement was maintained constant for 2 min, during which measurements, observations, and labeling of visible fractures were performed.

2.3 Instrumentation
Displacements, steel, and concrete stresses were evaluated at critical places of the tested 3D assemblies. Displacement was measured using six electrical linear variable distance transducers (LVDTs) with 0.01 mm precision, as illustrated in Fig. 8. The steel strain was measured using five electrical strain gauges (SG) of 10 mm gauge length and 120 Ohm resistance. A computer-controlled data acquisition system was used to link all LDVTs and strain gauges. The fracture patterns were

continually monitored and written on the walls, along with the accompanying displacement level.

3 Experimental Observations and Discussion
3.1 Un-strengthened 3D Assembly Behavior and Failure Pattern
Front and rear elevations of the un-strengthened 3D assemblies are shown in Figs. 9 and 10, these figures present the first fracture patterns for sample (S0-1), the crack present diagonal shear fractures at masonry panel bed-joints surrounding apertures. The first apparent fracture formed at 6.00 mm lateral displacement and 80 kN lateral stress in both push and pull directions. At this loading stage, no apparent fractures were seen on out-of-plane solid walls (side elevations).

The diagonal shear fractures around apertures expand as the applied lateral displacement increases for the in-plane loaded altitudes (front and back). The out-of-plane walls (left and right sides) act with their out-of-plane stiffness and strength until they begin to crack at high displacement, as seen in Figs. 11, 12, 13.

The un-strengthened assembly's failure pattern may be defined by shear failure with diagonal struts developing in the two piers encompassing both masonry units and confining columns/beams connections at both story levels, as illustrated in Figs. 11, 14. It is worth noting that no separation was seen at the toothed contact between
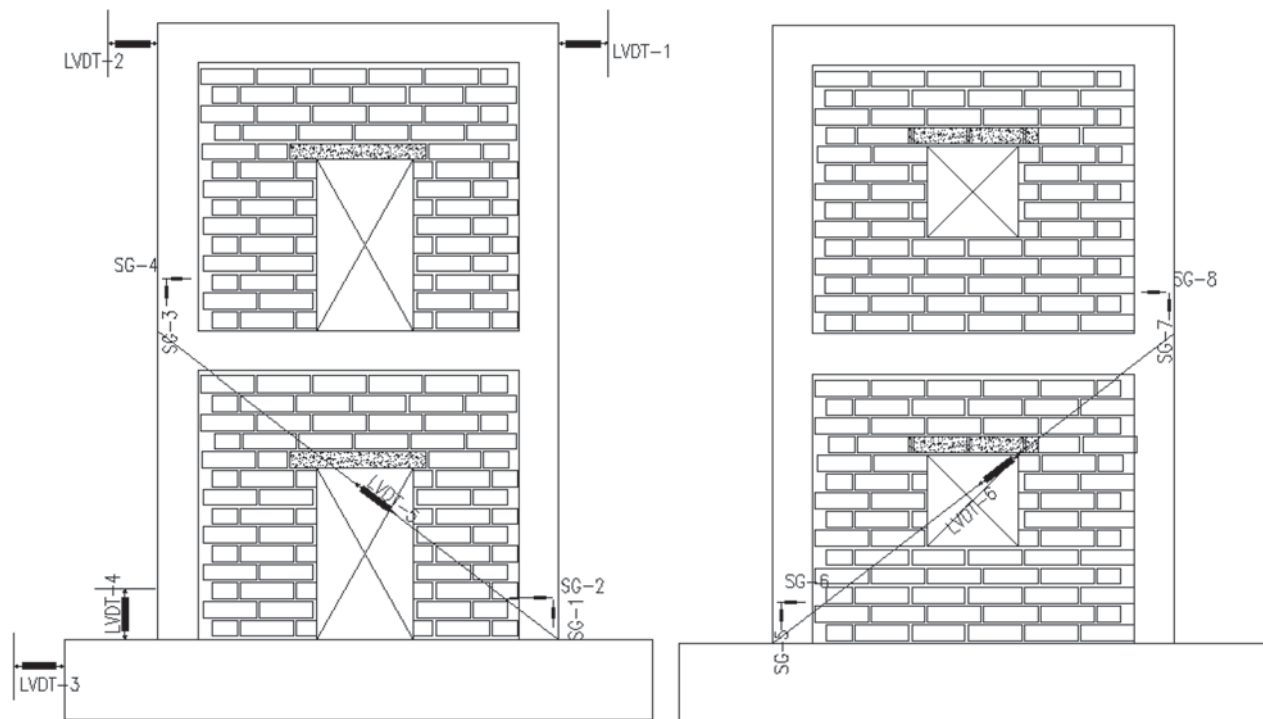

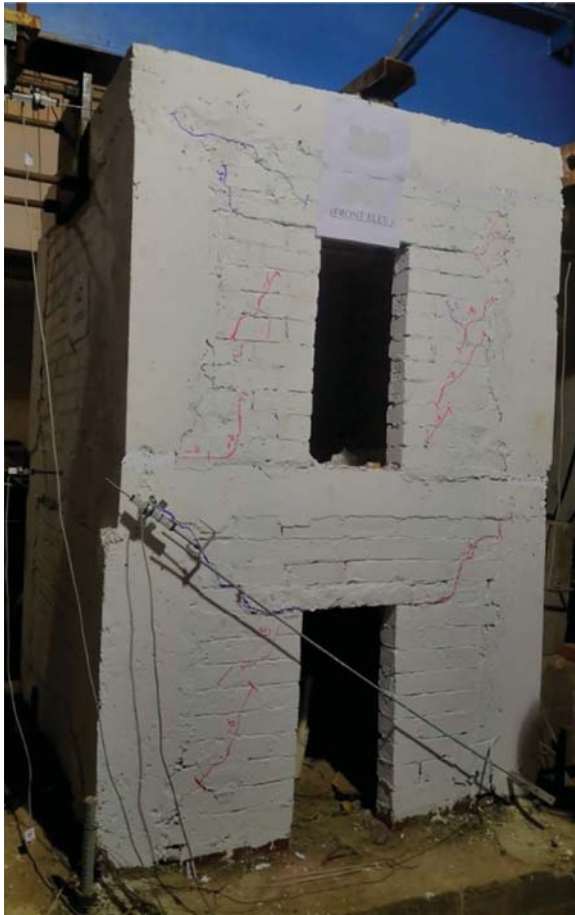**Fig. 8** Instrumentation scheme (front elevation/ back elevation)

El-Diasity *et al. Int J Concr Struct Mater*   (2023) 17:70

Page 8 of 30

Fig. 9 The first obvious cracks S-01 (front)

Fig. 10 The first obvious cracks S-01 (back)

the confining columns and the masonry panel, indicating that there is a major difference between in-filled frames and confined masonry panels.

3.2 The Failure Pattern and Behavior of a Strengthened 3D Assembly

S-02 building assembly was upgraded with a single coat of ferrocement covering the whole masonry panel, including confining components. Figs. 15 and 16 depict front and rear elevations of the first evident fracture patterns; diagonal shear cracks begin around apertures. The first apparent fracture formed at lateral displacement of 8.00 mm at top story with story drift of 0.0035 and lateral load of 200 kN, 210 kN in the push and pull directions, respectively. At this loading stage, no apparent fractures were seen on out-of-plane solid walls (side elevations).

As illustrated in Figs. 17, 18, the failure pattern of the strengthened assembly may be characterized by pure shear failure with diagonal fractures around apertures that completely detach the coupling component above the door/window at higher level.

The diagonal shear fractures around apertures expand as the applied lateral displacement increases for the in-plane loaded altitudes (front and back). Figs. 19, 20 demonstrate how the out-of-plane walls (left and right sides) behave with their out-of-plane stiffness and strength until they begin cracking at considerable displacement as visible cracks form horizontally (bending stresses).

The suggested upgrading approach raised the lateral resistance of the restricted assembly by approximately (61–95%), decreased the maximum lateral drift at failure by about (23–31%), but increased the corresponding load for the first visible fracture by about (150–175%). Furthermore, by retaining the wall integrity under substantial cyclic lateral loads for modified assembly walls (all sides, especially the perforated sides), collapse was greatly delayed.

Fig. 11 Crack failure pattern S-01 (back)

Fig. 21 depicts the hysteretic curve for both 3D assemblies, while Fig. 22 depicts the envelopes. Table 2 depicts the damage states and a summary of test findings for both un-strengthened and strengthened assemblies.

3.3 Energy Dissipation
Energy dissipation (ED) via hysteresis damping is a key feature in seismic design response and has been depicted as an area contained by the force–displacement curve at each displacement level (Hose & Seible, 1999). Fig. 23 shows a horizontally hatched region. In the same picture, the vertically hatched zone represents the elastic strain energy, Es, contained in an analogous linear elastic system.

Fig. 24 depicts that the max displacement at failure was decreased for the strengthened sample while the cumulative energy dissipation of 3D assemblies at various displacement levels was improved. According to the graph, a 27 percent improvement in total energy dissipation was obtained for the strengthened assembly S-02 compared to the un-strengthened assembly.
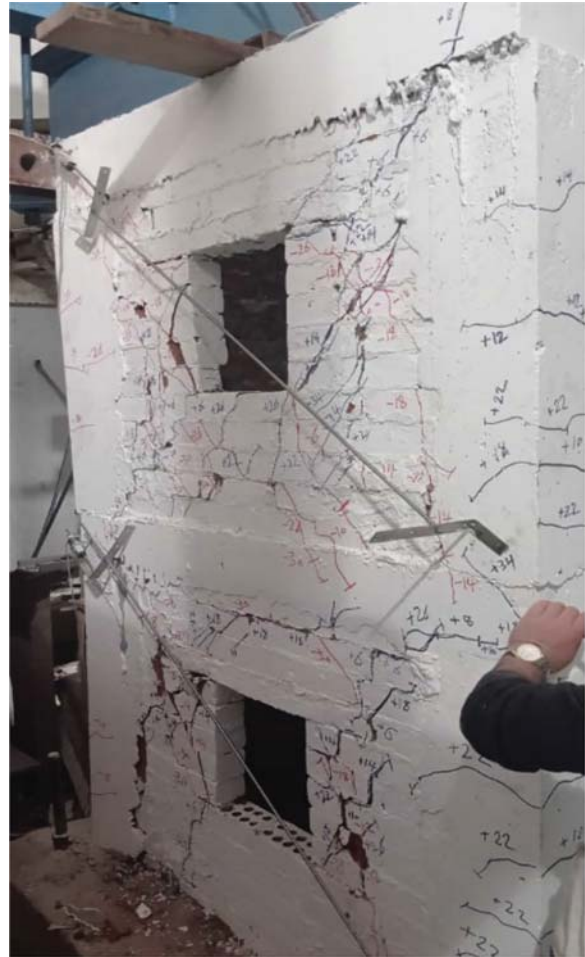
Fig. 12 Crack failure pattern S-01 (left)

3.4 Hysteretic Damping
The equal area technique (Hose & Seible, 1999) may be used to quantify hysteretic damping, which reflects the same amount of energy loss every loading cycle. The equation in Fig. 23 shows the link between the dissipated energy, Ed, the stored strain energy, Es, and the hysteretic damping.

Fig. 25 depicts the hysteretic damping vs. lateral top displacement for both 3D-assemblies S-01 and S-02. The hysteretic damping ranges between 6 and 10% for the unstrengthened assembly and 9–14% for the strengthened one. Also Fig. 25 shows that the damping ratio of the strengthened sample has been improved by 40%.

3.5 Stiffness Degradation
The secant stiffness, which is defined as the ratio of the lateral resistance to the top lateral wall displacement, this ratio have been used to measure the change in assembly building stiffness with the increasing loads and top

El-Diasity *et al. Int J Concr Struct Mater*   (2023) 17:70

Page 10 of 30
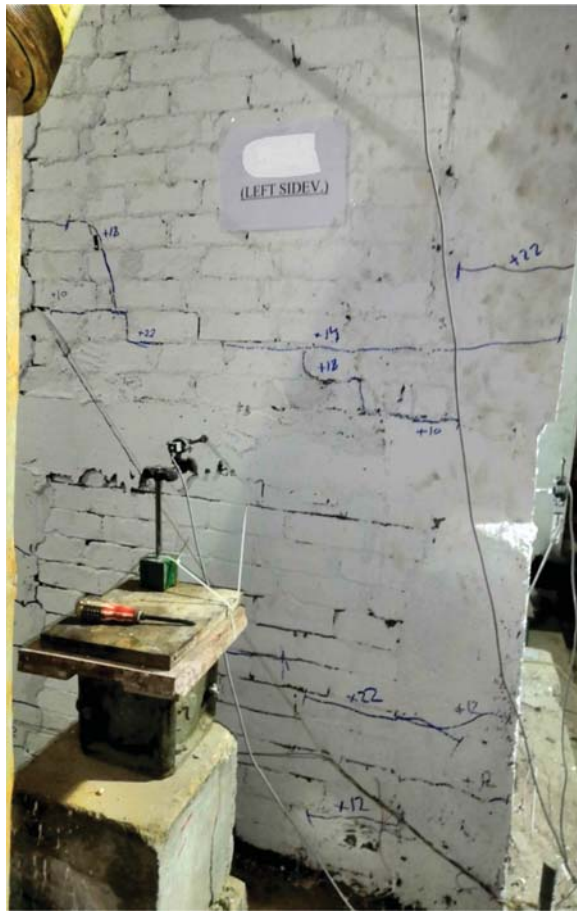
Fig. 13 Crack failure pattern S-01 (right)
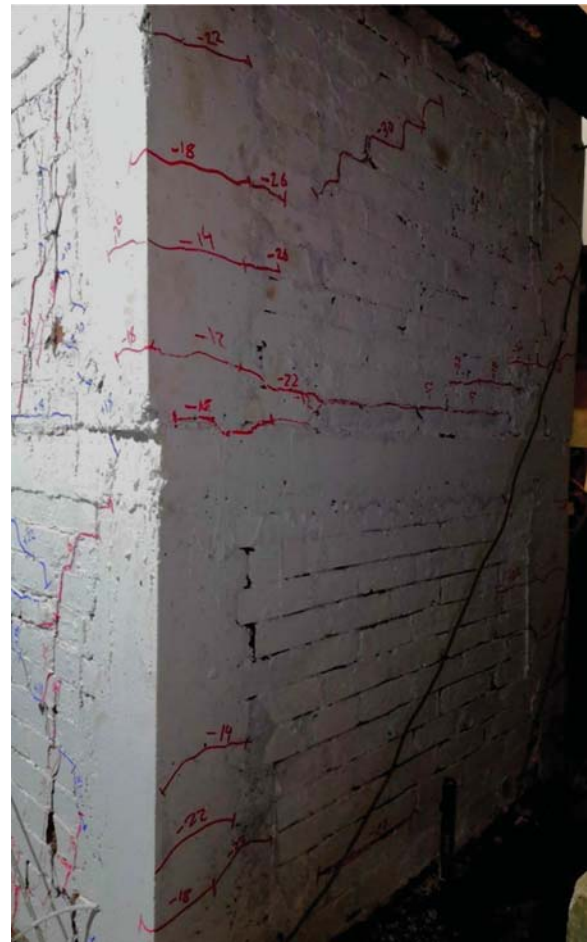
Fig. 14 Crack failure pattern S-01 (front)

displacement. As depicted in Fig. 26, the cycle stiffness of the specimen at a given displacement level was determined by averaging the stiffness in the positive and negative loading directions. Trends in the stiffness degradation of reinforced three-dimensional assemblies are revealing significant reductions with increasing top displacement. The rigidity of the reinforced assembly was increased by approximately 120 to 85% in relation to displacements between 5 and 25 mm.

4 Numerical Analysis

This section aims to develop a basic three-dimensional nonlinear model for the tested wall assemblies that is capable of capturing the essential response elements of the failure mode shapes and fracture patterns for each assembly and comparing them to experimental results and previous references.

In the past, numerous studies on finite element models of masonry walls and RC in-filled frameworks have been conducted. Kaushik et al. (2007) examined the uniaxial monotonic compressive stress–strain behavior of bricks,

mortar, and masonry and determined the modulus of elasticity to be 300, 200, and 550 times their compressive strengths, respectively.

Masonry is a heterogeneous material with a complex, non-linear, anisotropic behavior due to the different material components and presence of mortar joints. The complex irregular nature of masonry construction makes accurate structural analysis a challenge. Nonlinear analysis is considered to give better description for the behavior and capacity of masonry structures in many cases (Lourenco, 2002). To represent the heterogeneous and anisotropic nature of masonry construction using finite elements, different modeling strategies may be followed that are reviewed by Roca et al. (2010). Discretization of the structure can be performed using the following three approaches: (i) detailed micro-modeling, where masonry units and mortar joints are distinctly modeled as materials with different geometry and mechanical properties whereas the unit-mortar interface is represented by discontinuous interface elements accounting
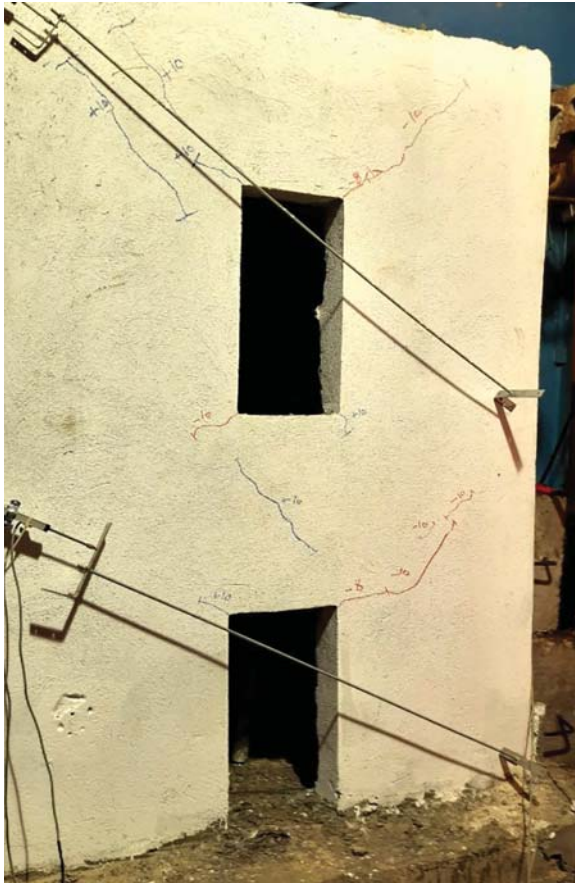
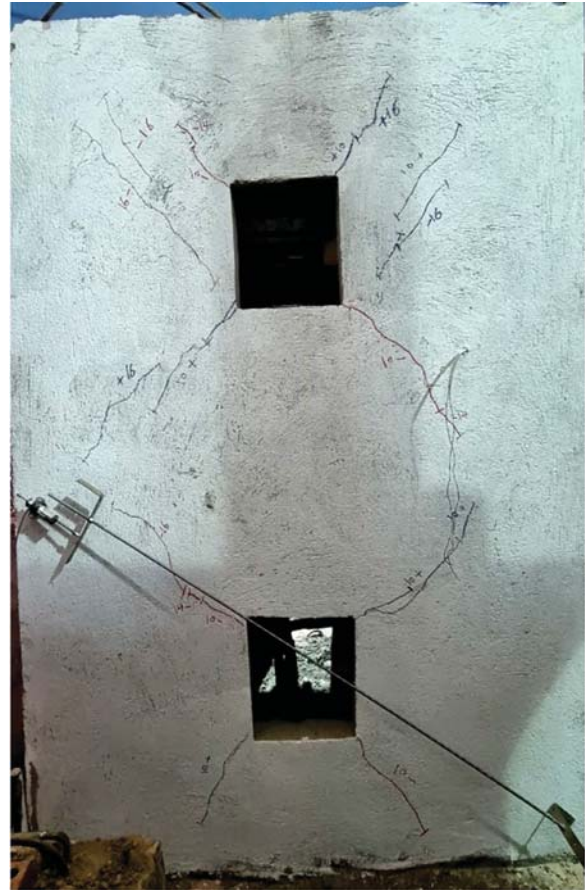**Fig. 15** The first obvious cracks S-02 (front)

Fig. 16 The first obvious cracks S-02 (back)

for possible crack or slip planes (Page, 1978); (ii) simplified micro-modeling, bricks are modeled by continuum elements while mortar joints are lumped in discontinuous interface elements (Singhal & Rai, 2018); (iii) macro-modeling, masonry is modeled as an isotropic continuum material characterized by different nonlinear softening laws in tension and compression (Lourenço et al., 2007). Comparison of the three main modeling strategies for masonry conclude that although detailed micro-models are capable of addressing some of the complexities, their application is primarily restricted to small-scale structures with regular geometric forms (Lourenco, 2002; Roca et al., 2010). The macro-modeling (smeared, continuum or homogenized) is more practice oriented due to the reduced time and memory requirements as well as a user-friendly mesh generation, and describes the structural behavior with acceptable accuracy (Roca et al., 2013). The smeared crack scalar damage models commonly used for reinforced concrete structures were also adapted for masonry historic buildings, where the damage is defined in a given point by a scalar value which defines the level of material degradation, and the cracking is considered as distributed along the structure (Milani, 2011; Yan et al., 2011).

Yan et al. (2011) studied the properties and characteristics of masonry utilizing Solid65 elements in "ANSYS®" (ANSYS® Academic Research, Release 12.0) and computationally simulated the shear property of joints in masonry structures subject to varying vertical loads (fm). By comparing experimental and numerical results, the recommended values for the shear transfer coefficients for open and closed cracks of Solid65 components for modeling masonry structures were determined.

4.1 Finite Element Model

The nonlinear finite element analysis was conducted using the computer program "ANSYS®" (ANSYS® Academic Research, Release 12.0). To idealize the concrete and masonry (SOLID65), an 8-node solid element with three translational and additional rotational degrees of freedom at each node was employed, while a 2-node bar element was used to represent the steel rebars (LINK8).

El-Diasity *et al. Int J Concr Struct Mater*   (2023) 17:70

Page 12 of 30

Fig. 17 Failure crack pattern S-02 (front)
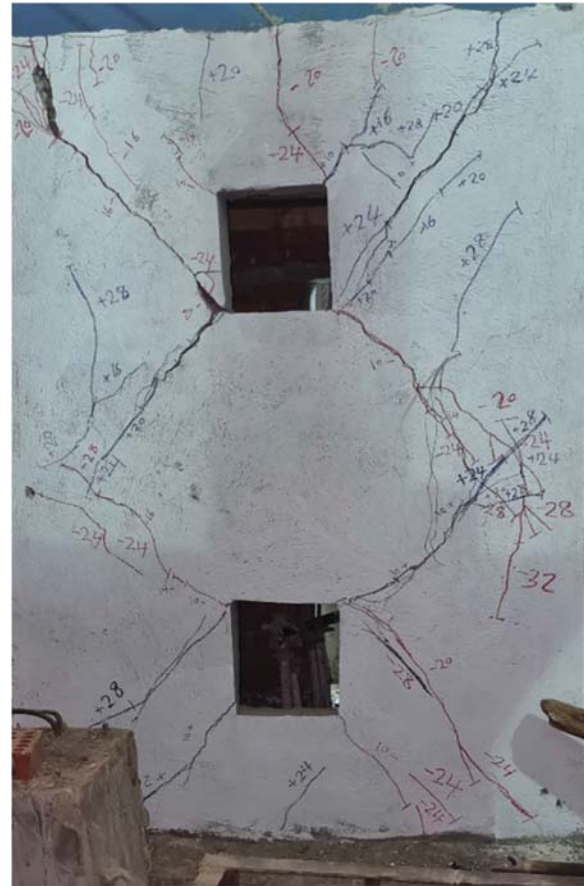
Fig. 18 Failure crack pattern S-02 (back)

Multilinear isotropic hardening material is used to simulate the masonry composite (brick and mortar) as well as the concrete elements. Iterative solution procedure based on the modified Newton–Raphson method was employed in order to simulate nonlinear behavior. The load is applied at 20 load steps; within each load step, equilibrium iterations are made until convergence criteria are satisfied and a converged solution is reached. Fig. 27 depicts a typical modeling of the column and beam components representing the concrete and steel reinforcing rods, in addition to the boundary conditions. The model was loaded in the same manner as the experimental program, with an incremental displacement cyclic load mounted on top of the assembly using the same displacement methodology as the experimental testing until failure occurred. As stated previously, no separation was observed at the toothed interface between the confining columns and the masonry panel under large deformation for all wall assemblies; therefore, the interface between the masonry panel and the concrete frame was modeled as a full bond with the corresponding mechanical properties for each material with respect to the stress strain curves for masonry suggested by Kaushik et al. (2007).

For multiaxial stress condition, the concrete material model in ANSYS employs a failure model established by Willam and Warnke (1975). Through this material model, the Solid65 element determines the cracking and crushing of concrete. Two or more material definitions may be combined to form a material model. Elastic and concrete material definitions should be included for concrete and masonry materials. Elastic definition requires the modulus of elasticity and Poisson's ratio. Axial tension strength for concrete and masonry, as well as shear transfer coefficients between crack surfaces for open and closed fractures, are needed for concrete definition. If there is no shear transfer from one fracture surface to the other, the shear transfer coefficient is 0.0; otherwise, the value is 1.0. There are several estimates for this coefficient in the literature by researchers (Sandeep et al., 2013; Tarek et al., 2020); the proposed values in this study were 0.3 and 0.6 for open and closed cracks in brickwork, respectively, as stated by Sandeep et al. (2013).

Fig. 19 Failure crack pattern S-02 (left)

Fig. 20 Failure crack pattern S-02 (right)

4.2 Implementation and Numerical Assessment

Comparisons of failure modes, cracking patterns, and plastic hinge positions, as well as load–displacement curves, are used to establish a link between experimental and numerical data.

The model's anticipated lateral load capacity and failure mechanism were compared to the test results for both assemblies. Fig. 28a and b illustrates the experimental and finite element model (FEM) load–displacement envelope curves for the un-strengthened assembly (S-01) and the strengthened assembly (S-02), respectively. Table 3 summarizes comparisons of maximum and ultimate loads with their related displacements for models and experimental data.

Fig. 29a–d for un-strengthened assembly and Fig. 30a–d for strengthened assembly demonstrate the cracking patterns for the finite element models for each 3d-assembly as compared to the experimental test findings.

Fig. 31 depicts the shear stresses at ultimate load for the unreinforced assembly (S-01), demonstrating that shear stresses in masonry panels have an average value of 0.8 MPa at the diagonal compression strut, which is close to the maximum derived shear stresses for tested wallets, where the calculated values for maximum shear stresses equal 0.78 MPa. At tie columns, shear stresses reach 1.22 to 0.80 MPa, which are the maximal shear stress values for reinforced concrete with an average compressive strength of 24.5 MPa.

Fig. 32 depicts the mechanical strain ultimate load, with the strain in masonry ranging from 0.0075 to 0.058, which is acceptable by the specified values determined and stated by Kaushik et al. (2007) as the proposed ultimate strain equals 0.027.

Fig. 33 illustrates shear stresses at maximum load for strengthened assembly (S-02), indicating that shear stresses in masonry panels have an average value of 1.824 MPa at the diagonal compression strut. Maximum shear stresses for reinforced concrete with an average compressive strength of 24.5 MPa range from 3.91 to 4.279 MPa at tie columns.

Fig. 34 depicts the mechanical strain at ultimate load, with the strain in masonry ranging from 0.0028 to 0.0293, which is acceptable by the specified values determined
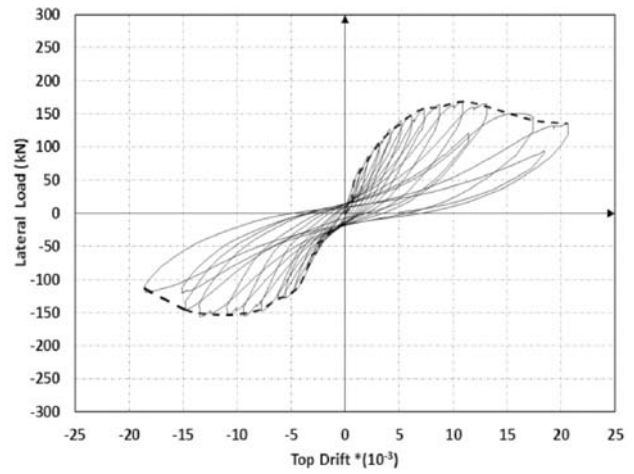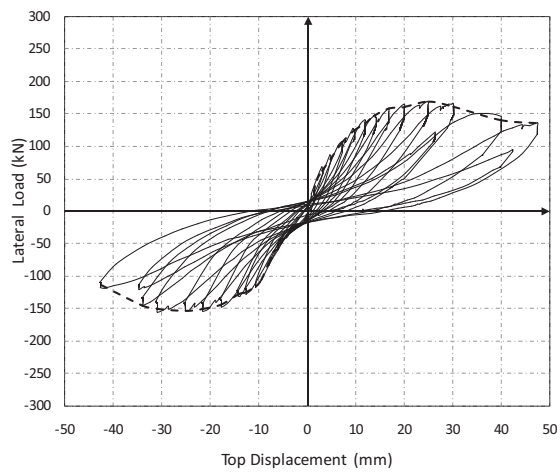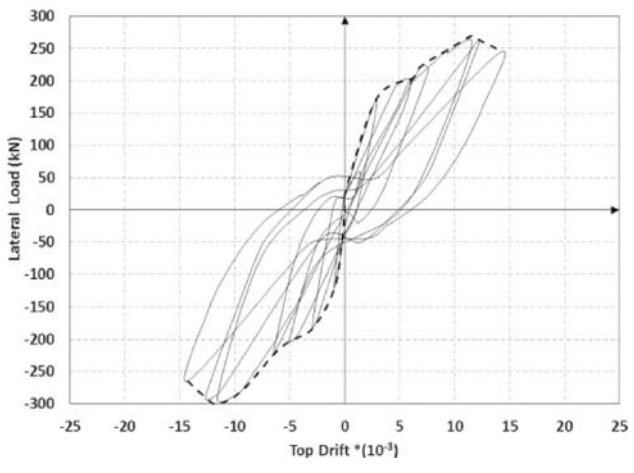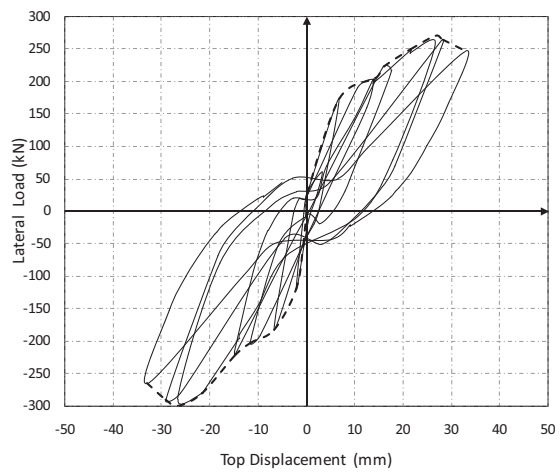
Fig. 21 Strengthened and un-strengthened assemblies' hysteretic curves. **a** Un-strengthened 3D assembly (S-01) ((Displacement and drift) **b** Strengthened 3D assembly (S-02) (Displacement and drift)
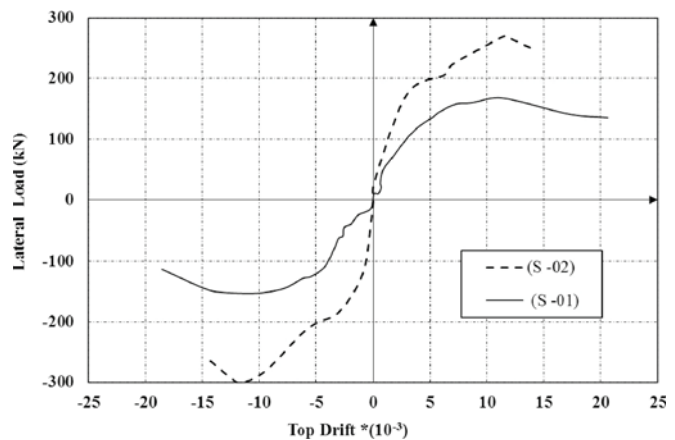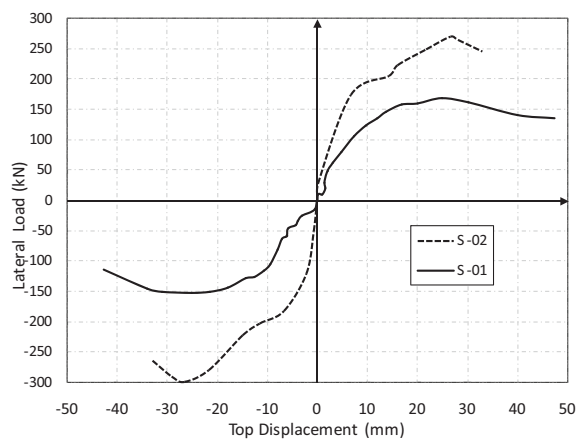

Fig. 22 Envelope curves for 3d assemblies (displacement and drift)

Table 2 Test results summary

Id	Direction	First visible cracks stage					Maximum load stage					Failure stage				
		Loads		Displacement at top story			Loads		Displacement at top story			Loads		Displacement at top story		
		Load (kN)	Var.%	Disp. (mm)	Var.%	Drift	Load (kN)	Var.%	Disp. (mm)	Var.%	Drift	Load (kN)	Var.%	Displ (mm)	Var.%	Drift
S-01	Push	+80	–	+6	–	0.0026	168	–	25	–	0.01	136	–	48	–	0.021
	Pull	− 80	–	− 6	–	0.0026	− 154	–	− 25	–	0.01	− 114	–	− 43	–	0.018
S-02	Push	200	150[#]	8	33[#]	0.0035	270	61[#]	27	8[#]	0.011	246	80[#]	33	− 31[#]	0.014
	Pull	− 220	175[#]	− 10	67[#]	0.0043	− 300	95[#]	− 27	8[#]	0.011	− 265	132[#]	− 33	− 23[#]	0.014

[#] % based on the specimen (S-01)
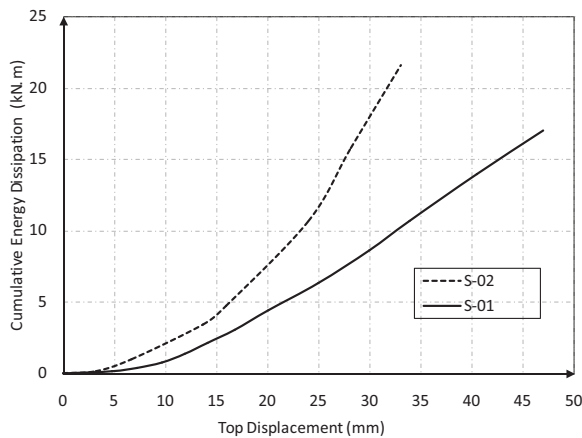
Fig. 23 Cumulative energy dissipation for assemblies
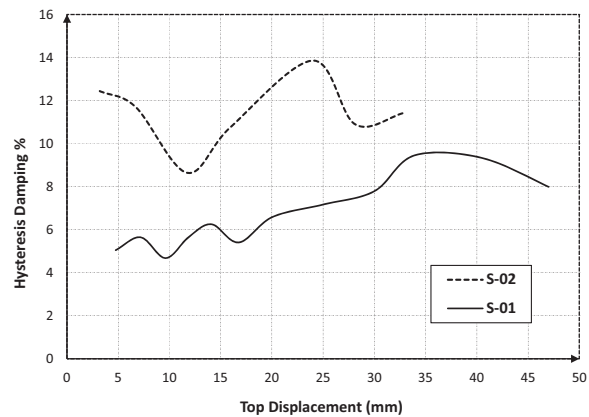
Fig. 25 Hysteresis damping percentage
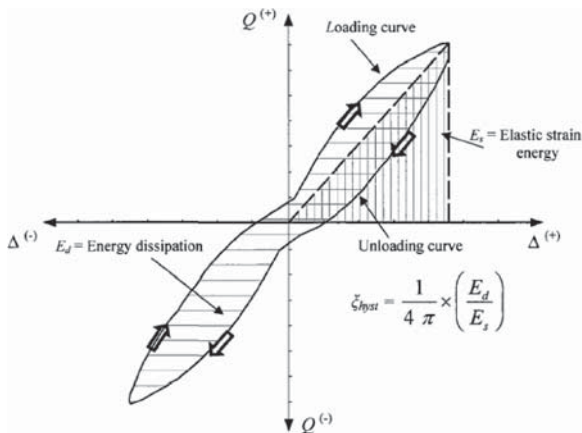
Fig. 24 Energy dissipation calculations (Hose & Seible, 1999)

and stated by Kaushik et al. (2007) as the proposed ultimate strain equals 0.027.

The results of the finite element analysis indicated that the created models are accurate enough to predict the maximal load and its associated deformation of the tested assemblies. Model displacements were smaller than experimental displacements, indicating that the plastic analysis needs improvement. As shown in figures, the proposed model corresponds good agreement with laboratory test results for fracture patterns and failure mechanisms for all models.

5 Parametric Study

A parametric study is performed to investigate the lateral load capacity and crack patterns for both in-plane and out of plane of a 3d building with dimensions mentioned before in this study, many parameters have been considered using the non-linear finite element models as listed in Table 4. The different parameters included in the study are number of stories, number of bays, exist of openings in walls, no. of ferrocement layers, out-of-plane loading and the longitudinal and transverse reinforcement of tie column.

For retrofitted sample, the effect of number of stories related to the number of bays is presented in Fig. 35 and
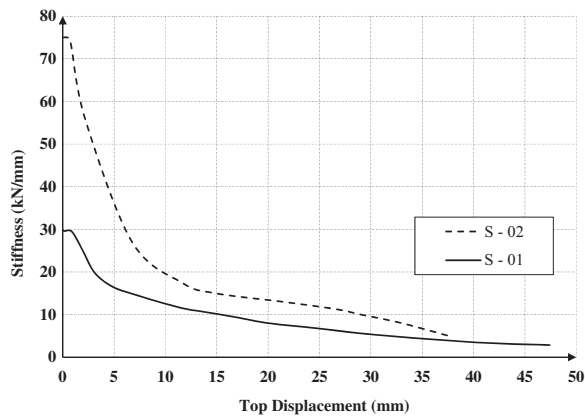
Fig. 26 Stiffness degradation for assemblies

it was concluded that lateral load capacity of the building decreases with the increasing number of stories also the increasing number of bays increase the global stiffness of the building and relatively increase the lateral capacity of the structure. Fig. 36 shows that the strengthening of all sides of wall increase the load capacity by approximate 38% while the gained percentage of increase is about 11% when strengthening take place for each of front/back and side walls separately. The longitudinal reinforcement of the tie column slightly increases the load capacity by 20% when using 4T16 reinforcement rather than 4T10 reinforcement as shown in Fig. 37a while transfer reinforcement of the tie column almost did not affect the load capacity of the building, as shown in Fig. 37b.

Damage state analysis for the results of the parametric study has been implemented to illustrate the performance
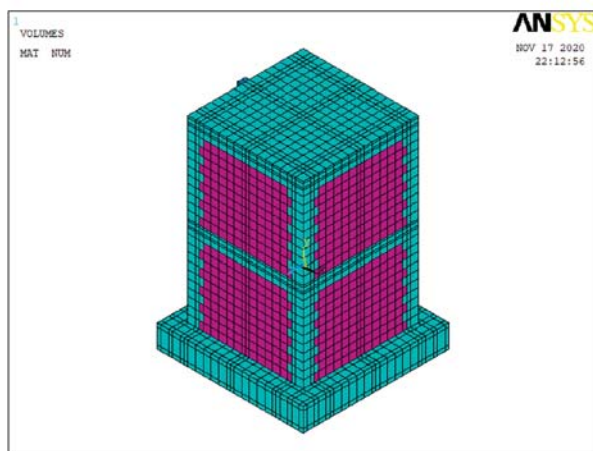
(a)
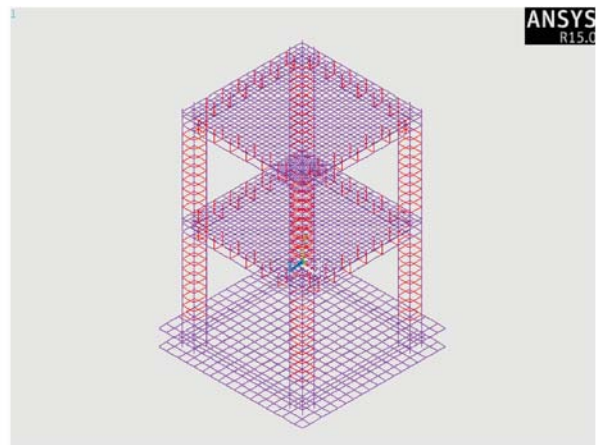
(b)
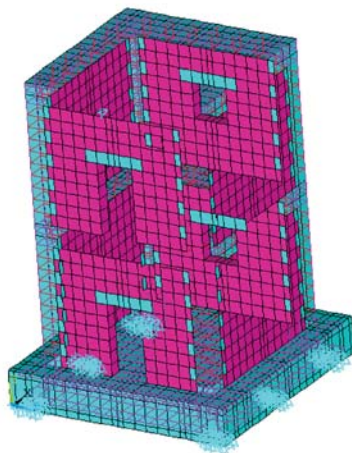
(c)
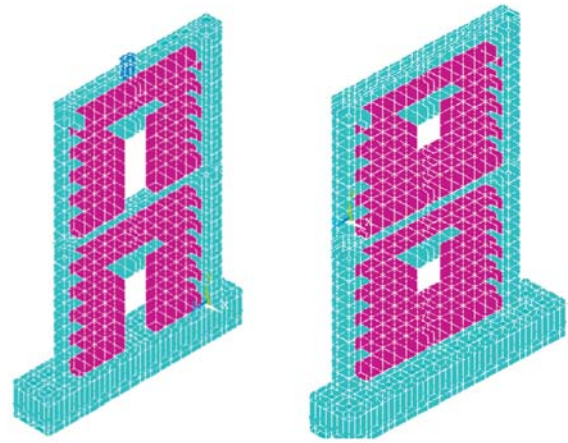
(d)

Fig. 27 Finite element model characterization and meshing (**a**), rebar (**b**), (**c**) boundary conditions, (**d**) meshing of perforated walls
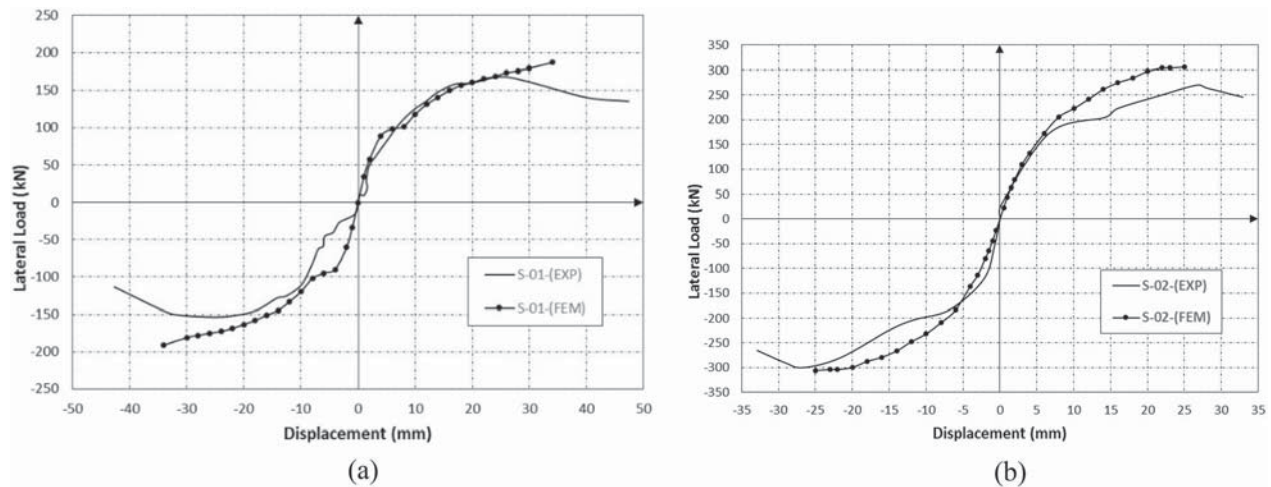
Fig. 28 (**a**) Envelope load–displacement curves for building assembly S-01, (**b**) Envelope load–displacement curves for building assembly S-02

of the building under lateral cyclic loading until failure. The damage states can be classified as small damage (DS1) in which minor cracks start to appear in the walls of the building, moderate damage (DS2) in which flexural cracks appear in the R.C confining elements, sever damage (DS3) in which large diagonal cracks appear in the masonry walls and load capacity reaches maximum value and final damage state is collapse of the building (DS4) in which shear failure occur in the R.C confining elements and sliding or rocking failure may occur.

The fragility curves for the masonry building are used to know the probability that a particular damage will occur in the elements of the building. The top drift ratio of the building at each model is selected to be the demand parameter. Fragility functions are mainly used to study the uncertainty concerned with specific materials and different elements configurations.

The ATC-58-1 (ATC-58-1, 2011)) recommends the use of a cumulative probability function based on a log-normal probability distribution for the generation of fragility functions. The log-normal probability distribution function is shown in Eq. 2 and requires determination of the median value (drift ratio or moment at base per unit length) for each damage state (xm) as well as

the logarithmic standard deviation or dispersion (βi) as determined by Eqs. 3 and 4, respectively (Bhargavi & Pradeep, 2015; Shanour et al., 2014) (Table 5) (Fig. 38).

$$x_m = \exp(\frac{1}{M}\sum_{i=1}^{M}\ln r_i), \tag{2}$$

$$\beta = \sqrt{\frac{1}{M-1}\sum_{i=1}^{M}(\ln(r_i/x_m))^2}, \tag{3}$$

$$F_{dm}(edp) = \Phi\left(\frac{\ln(edp/x_m)}{\beta}\right). \tag{4}$$

6 Conclusions and Summary

The findings of lateral cyclic loading testing on a two-story confined masonry structure utilizing local materials and standards are presented in this study. Two half-scale confined masonry structures were constructed using a clay masonry panel, confining columns, tie beams, and recusals. The assemblies were tested up to failure using a
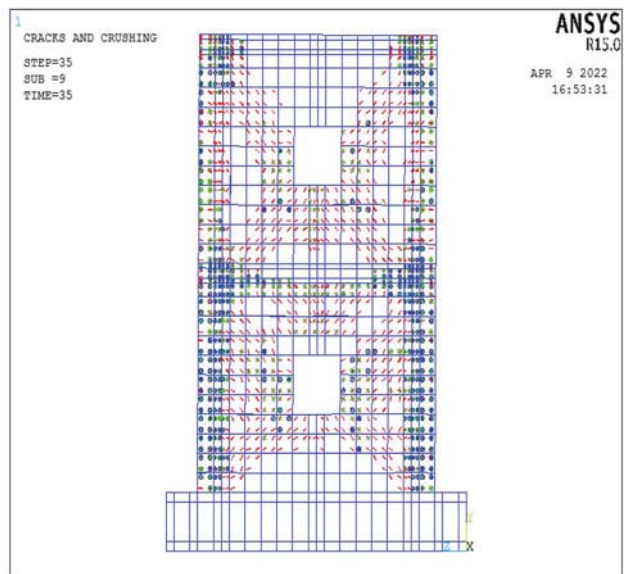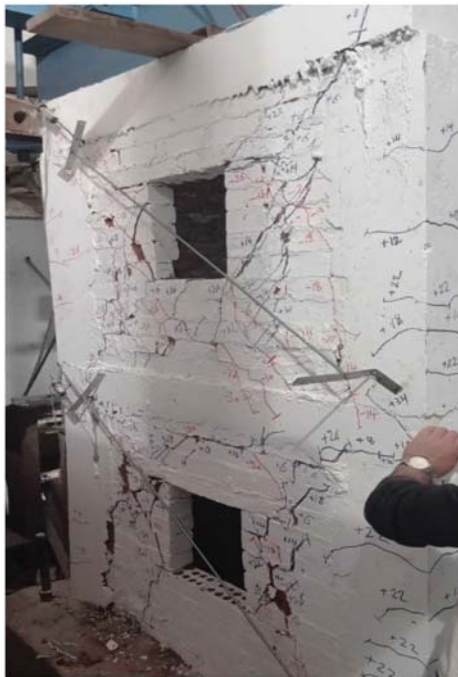
Table 3 A comparison of the finite element model and the test findings

Assembly ID	Direction	Max. load (kN)			Displacement in relation to the maximum load (mm)			Load cracking (kN)			Max. displacement (mm)		
		Exp	F.E.M	Exp. / F.E.M.	Exp	F.E.M	Exp. / F.E.M.	Exp	F.E.M	Exp. / F.E.M.	Exp	F.E.M	Exp. / F.E.M.
S-01	Push	168	187	0.89	25	34	0.74	80	100	0.80	48	34	1.41
	Pull	− 154	− 182	0.85	− 25	− 34	0.74	− 80	− 105	0.76	− 43	− 34	1.26
S-02	Push	270	306	0.88	27	20	1.35	200	220	0.90	33	25	1.65
	Pull	− 300	− 306	0.98	− 27	− 20	1.35	− 220	− 230	0.95	− 33	− 25	1.65

El-Diasity *et al. Int J Concr Struct Mater* (2023) 17:70

Page 18 of 30

a

b

Fig. 29 (**a**) Crack pattern at ultimate load for (S-01)—front elevation (experimental/FEM), (**b**) Crack pattern at ultimate load for (S-01)—back elevation (experimental/FEM), (**c**) Crack pattern at ultimate load for (S-01)—left side view (experimental/FEM), (**d**) Crack pattern at ultimate load for (S-01)—right side vie (experimental/FEM)
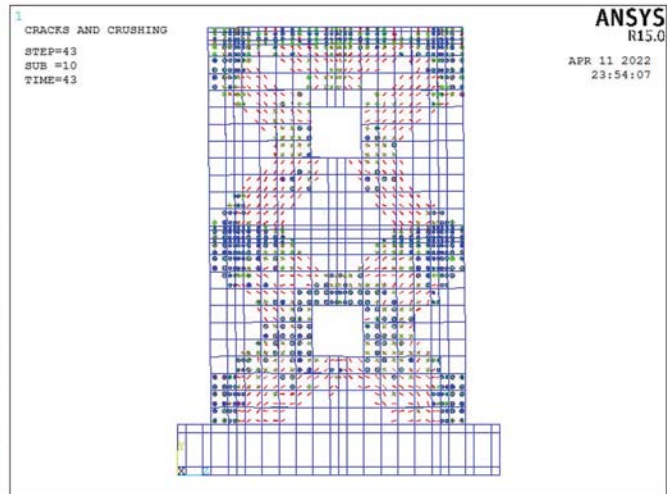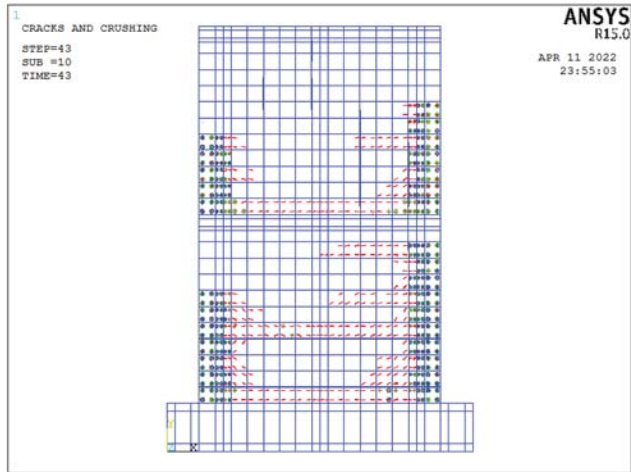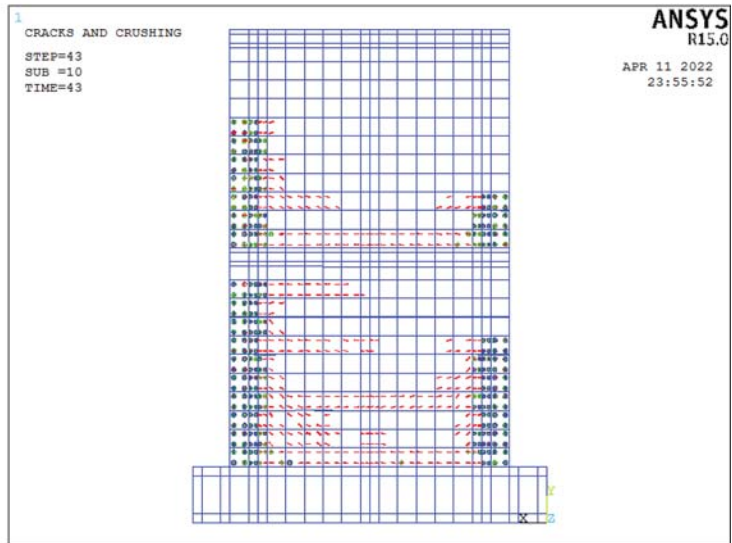
*red line represent cracks - green and blue lines represent crushing

c

*red line represent cracks - green and blue lines represent crushing

d

Fig. 29 continued

*red line represent cracks - green and blue lines represent crushing

a

*red line represent cracks - green and blue lines represent crushing

b

Fig. 30 (**a**) Crack pattern at ultimate load for (S-02)—front elevation (experimental/FEM), (**b**) Crack pattern at ultimate load for (S-02)—back elevation (Experimental/FEM), (**c**) Crack pattern at ultimate load for (S-02)—left side view (experimental/FEM), (**d**) Crack pattern at ultimate load for (S-02)—right side view (experimental/FEM)

*red line represent cracks - green and blue lines represent crushing

c

*red line represent cracks - green and blue lines represent crushing

d

Fig. 30 continued

El-Diasity *et al. Int J Concr Struct Mater* (2023) 17:70
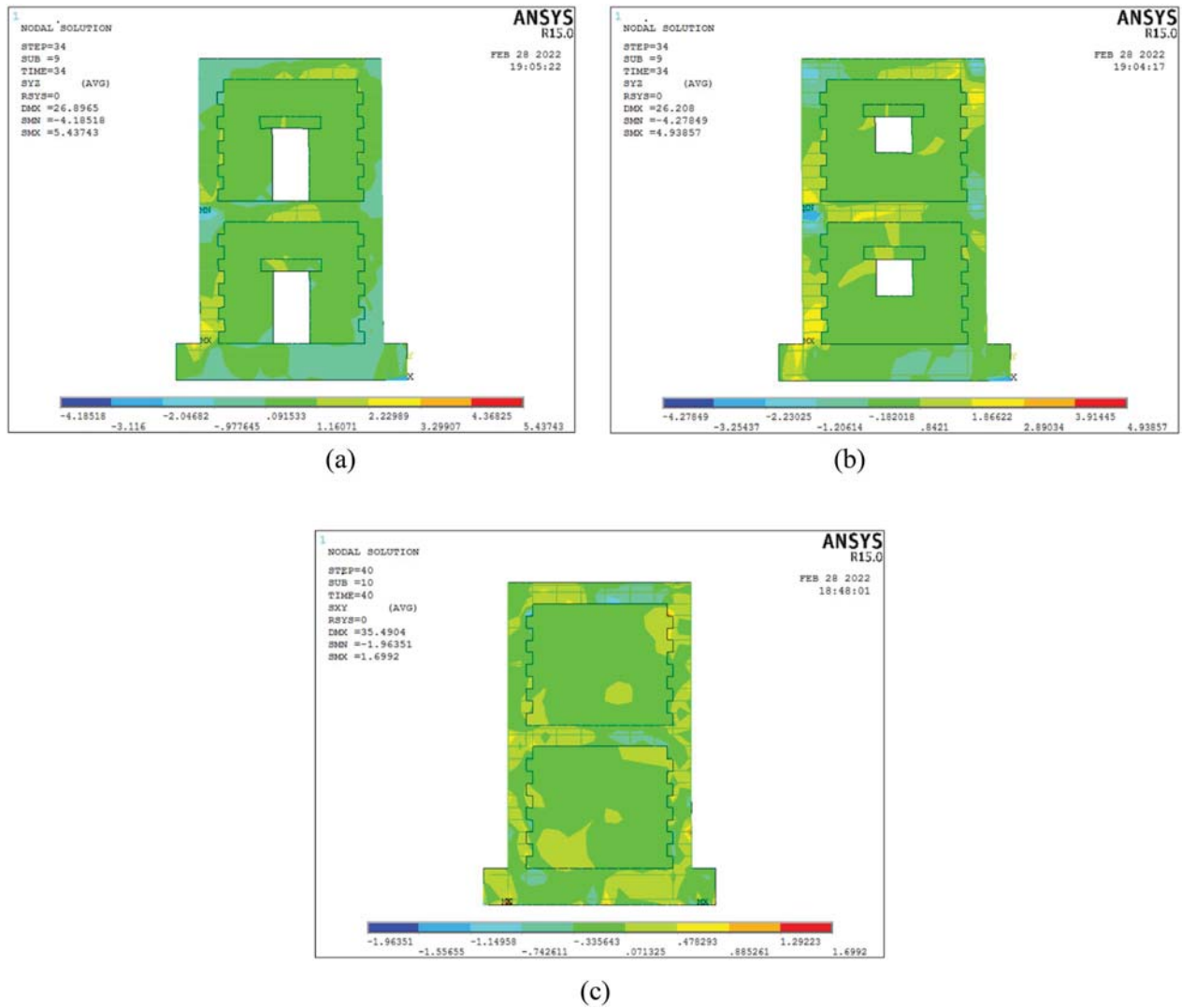
Page 22 of 30
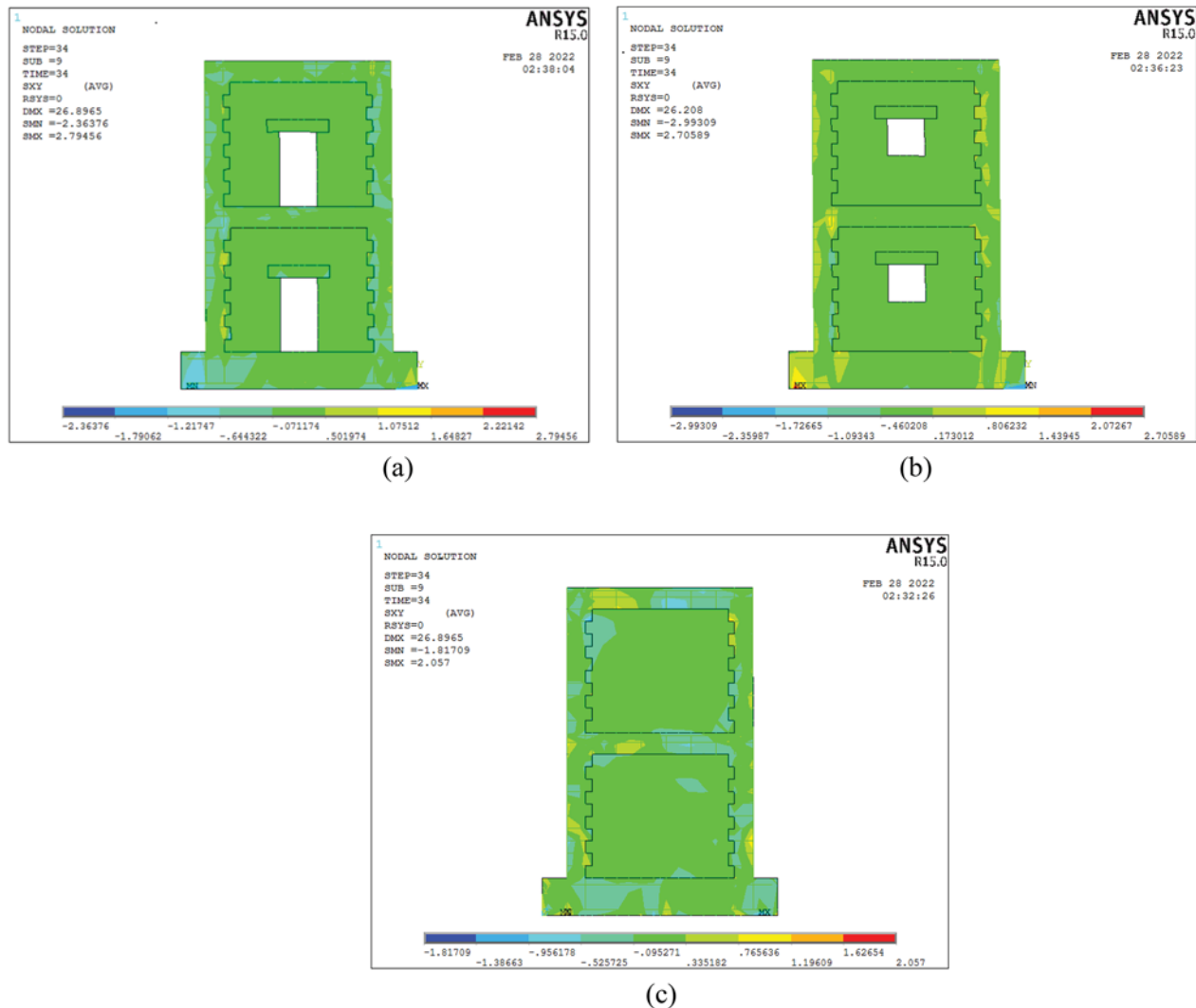
Fig. 31 Shear stress (in MPa) at ultimate load for (S-01) (**a**) front elevation (**b**) back elevation, (**c**) left / right side view

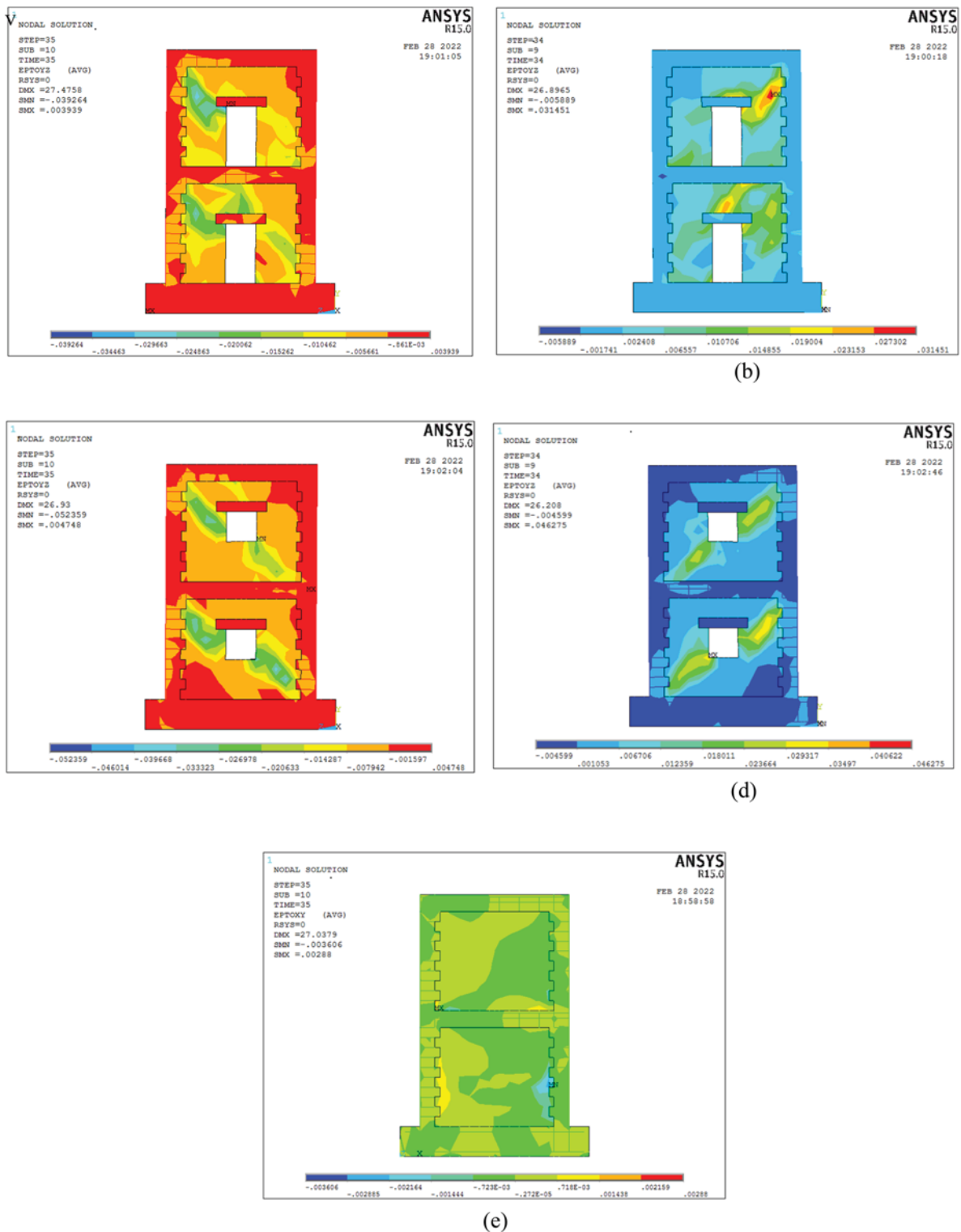displacement controlled loading methodology under vertical self-weight and lateral reversed cyclic loading. The walls of the assemblies have varying perforations (solid/windows/doors) to examine the influence of perforation on in-plane and out-of-plane performance. A strengthened assembly with an exterior layer of ferrocement was also examined. The following are some key study findings:

1. Shear failure with diagonal struts developing in the two piers containing both masonry units and confining columns/beams connections at both story levels may define the failure pattern of the un-strengthened

assembly. It should be noted that no separation was seen at the toothed contact between the confining columns and the masonry panel, indicating a substantial difference between in-filled frames and confined masonry panels.

2. The strengthened assembly's failure pattern may be characterized by pure shear failure with diagonal fractures around apertures that completely separate the coupling component above the door/window at the higher level.

3. The suggested upgrading approach increased the lateral resistance of the confined assembly by about
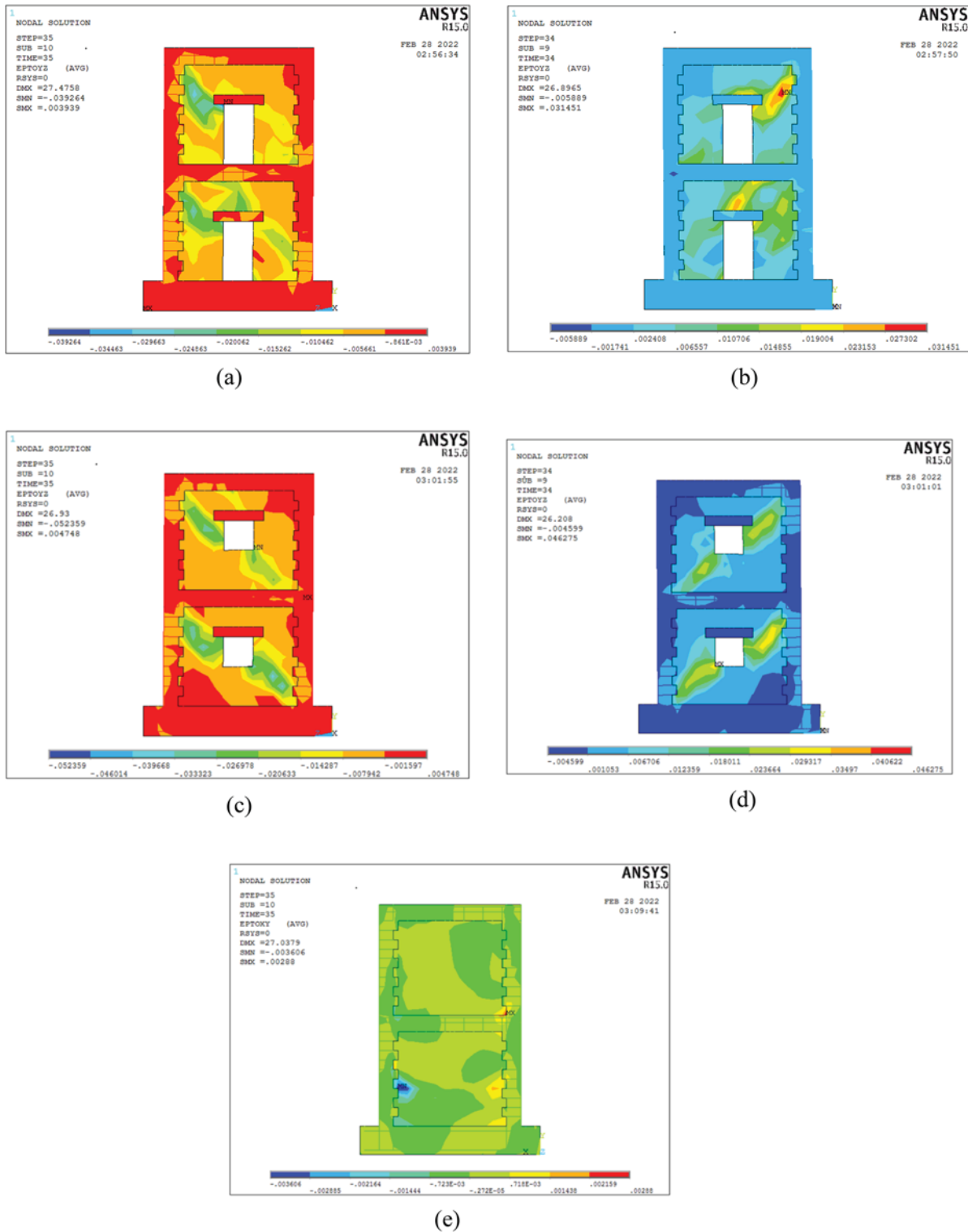
Fig. 32 Mechanical strain at ultimate load for (S-01), (**a**) front elevation at push loading, (**b**) front elevation at pull loading, (**c**) back elevation at push loading, (**d**) back elevation at pull loading, (**e**) left / right side view

El-Diasity *et al. Int J Concr Struct Mater*   (2023) 17:70

Page 24 of 30

Fig. 33 Shear stress (in MPa) at ultimate load for (S-02), (**a**) front elevation, (**b**) back elevation, (**c**) left / right side view

Fig. 34 Mechanical strain at ultimate load for (S-02), (**a**) front elevation at push loading, (**b**) front elevation at pull loading, (**c**) back elevation at push loading, (**d**) back elevation at pull loading, (**e**) left / right side view

El-Diasity *et al. Int J Concr Struct Mater*   (2023) 17:70

Page 26 of 30

Table 4 Summary of parametric study applied on the building

Parametric study						
No. of stories	No. of bays			Strengthening location of different wall sides	Longitudinal rft of tie columns	Shear links of tie columns
	One bay	Two bay	Three bay			
One story	One story	One story	One story	Un-retrofitted specimen	4T10	T6@200
Two story	Two story	Two story	Two story	Retrofitted- full coverage specimen	T124	T8@200
Three story	Three story	Three story	Three story	Retrofitted- front and back only specimen	T164	T10@200
Four story	Four story	Four story	Four story	Retrofitted- side walls only specimen		
Five story	Five story	Five story	Five story			
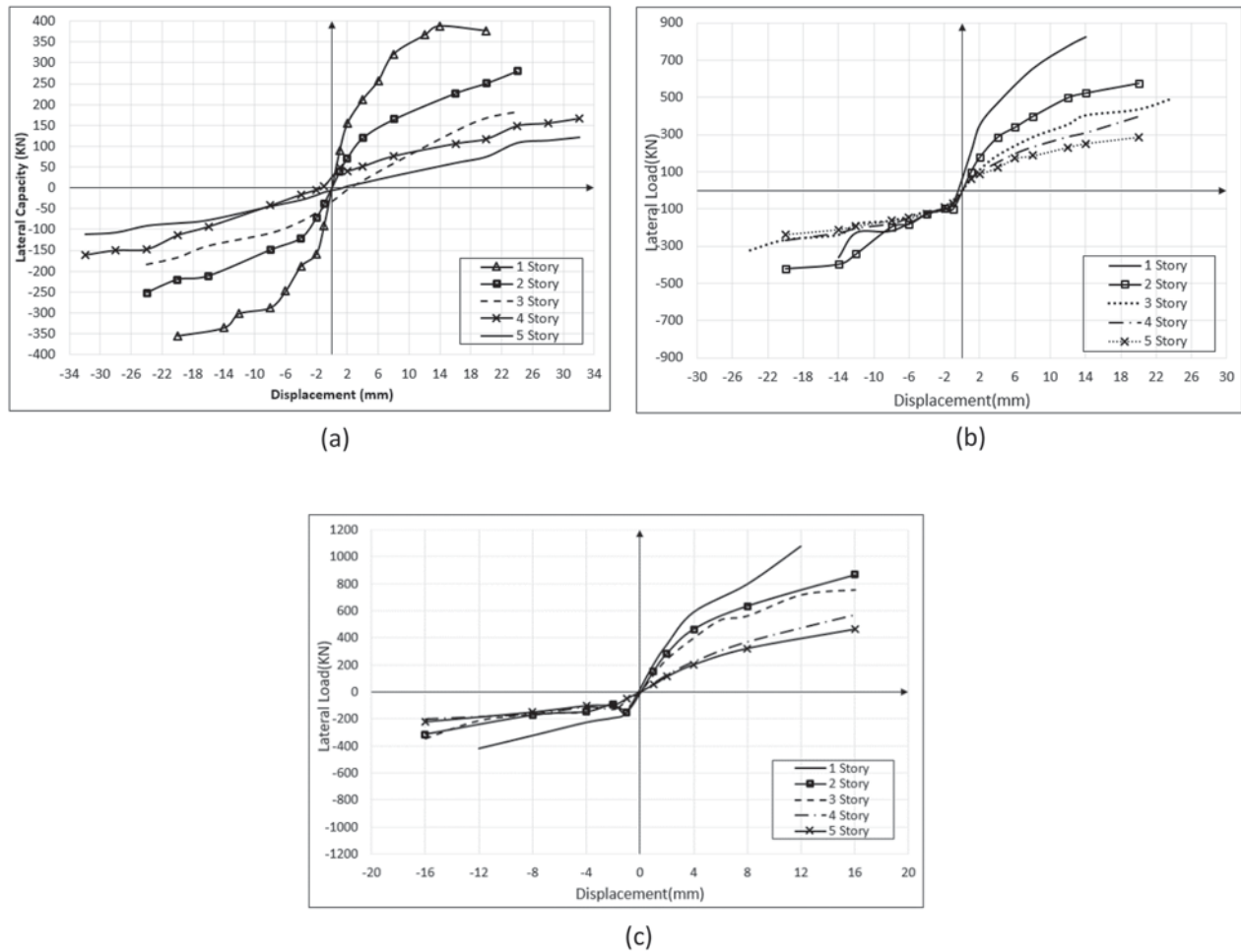
Fig. 35 a One-bay building, **b** two-bay building, **c** three-bay building
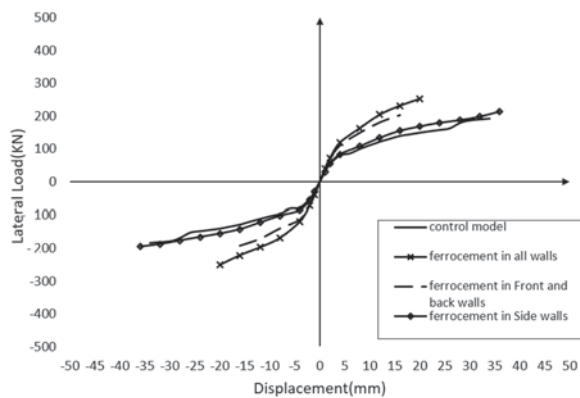
Fig. 36 Strengthening location of different wall sides (front and side walls)

(61–95%) while improving the ductility and total energy absorbed by 27%.

4. The maximum lateral drift at failure was lowered by about (23–31%), however the corresponding load for the first apparent fracture was raised by approximately (150–175%).

5. By maintaining the wall integrity under high cyclic lateral loads, collapse of strengthened assembly walls (all sides, especially the perforated sides) was greatly delayed.

6. In most cases, the provided finite element models agreed well with the findings of laboratory testing for maximum load and related deformation.

Fig. 37 **a** Longitudinal reinforcement, **b** transverse reinforcement of the tie columns

Table 5 The damage state of the studies buildings

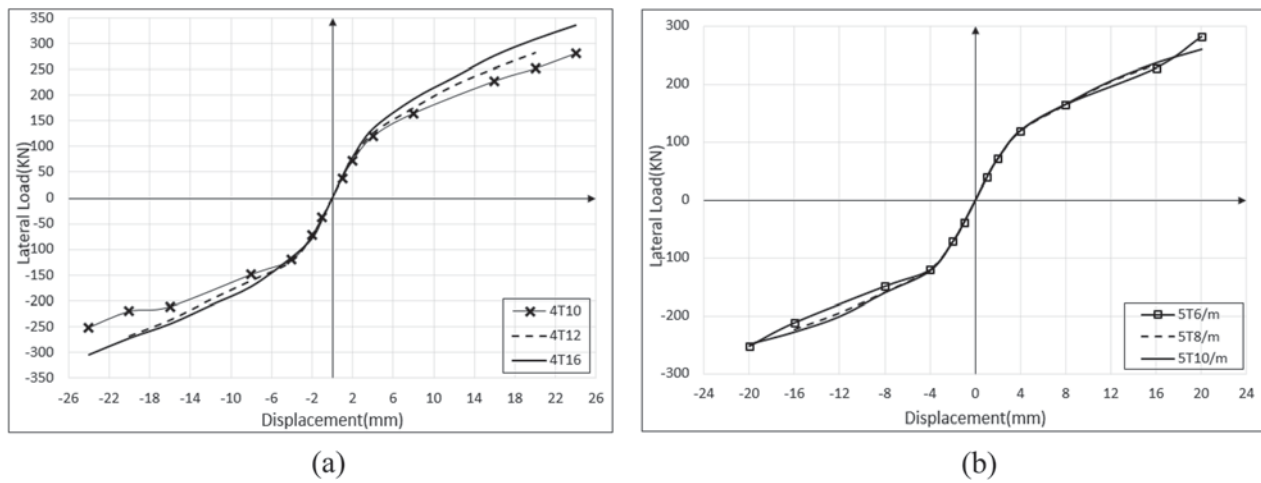| Damage state			DS1		DS2		DS3		DS4	
STORY	BAY	Direction	Load (kN)	Drift ratio (%)	Load (kN)	Drift ratio (%)	Load (kN)	Drift ratio (%)	Load (kN)	Drift ratio (%)
1 Story	1 Bay	Pull	89	0.06	155	0.137	389	0.96	378	1.38
		Push	− 90	− 0.06	− 159	− 0.137	− 355	− 1.38	− 355	− 1.38
	2 Bays	Pull	207	0.07	352	0.16	825	0.96	825	0.96
		Push	− 70	− 0.07	− 107	− 0.16	− 362	− 0.96	− 362	− 0.96
	3 Bays	Pull	198	0.06	346	0.137	1076	0.83	1076	0.83
		Push	− 155	− 0.05	− 195	− 0.137	− 421	− 0.83	− 421	− 0.83
3 Story	1 Bay	Pull	20	0.026	136	0.426	182	0.64	182	0.64
		Push	− 46	− 0.026	− 139	− 0.426	− 184	− 0.64	− 184	− 0.64
	2 Bays	Pull	57	0.03	109	0.053	498	0.64	498	0.64
		Push	− 57	− 0.03	− 109	− 0.053	− 324	− 0.64	− 324	− 0.64
	3 Bays	Pull	128	0.026	245	0.053	758	0.426	758	0.426
		Push	− 126	− 0.026	− 147	− 0.106	− 347	− 0.426	− 347	− 0.426
5 Story	1 Bay	Pull	60	0.264	108	0.396	121	0.53	121	0.53
		Push	− 78	− 0.264	− 92	− 0.396	− 112	− 0.53	− 112	− 0.53
	2 Bays	Pull	87	0.033	122	0.066	287	0.33	287	0.33
		Push	− 93	− 0.033	− 127	− 0.066	− 238	− 0.33	− 238	− 0.33
	3 Bays	Pull	56	0.017	115	0.07	465	0.264	465	0.264
		Push	− 48	− 0.017	− 94	− 0.07	− 218	− 0.264	− 218	− 0.264

El-Diasity *et al. Int J Concr Struct Mater*   (2023) 17:70
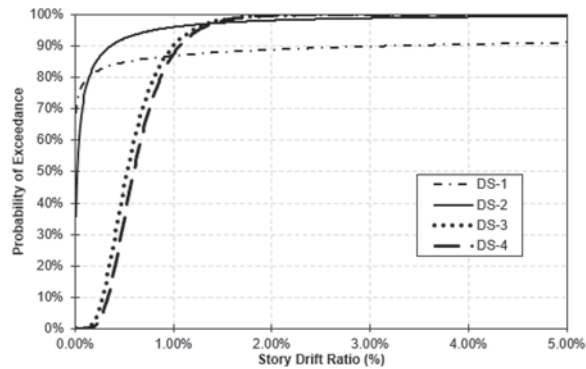
Page 29 of 30

Fig. 38 Drift fragility curve for the building

7. The agreement of results of the half-scale experimental model with the same scale FEM, help in using the FEM for design of different and full scale structures.
8. To improve the strengthened sample and decay the separation of coupling beam from the piers, additional layer of expanded shall be applied locally as the coupling beam zone, or increasing the thickness of the expanded wire mesh at the same zone.

Declarations

Ethics approval and consent to participate
Not applicable.

Consent for publication
Not applicable.

Competing interests
There is no competing interest associated with the submission of this manuscript.

References
ANSYS® Academic Research, Release 12.0, ANSYS, Inc.

Ashraf, M., et al. (2012). Seismic behavior of unreinforced and confined brick masonry walls before and after ferrocement overlay retrofitting. *International Journal of Architectural Heritage, 6*, 665–688.
ASTM E519-02. (2002). Standard test method for diagonal tension (Shear) in masonry assemblages.
ATC-58-1. (2011). Seismic performance assessment of building. Volume 1, prepared by ATC for FEMA.
Bhargavi, S., & Pradeep Kumar, R. (2015). Comparison between the effect of lintel and lintel band on the global performance of load bearing walls and masonry infilled RC frames. *International Journal of Civil Engineering and Technology, 6*(2), 68–78.
Choayb, B., Jean-Patrick, P. L. A. S. S. I. A. R. D., Messabhia, A., Ple, O., & Guenfoud, M. (2021). Analytical and numerical study of double-panel confined masonry walls. *Journal of Building Engineering., 39*, 102322. https://doi.org/10.1016/j.jobe.2021.102322
Chourasia, A., et al. (2019). Experimental investigation of seismic strengthening technique for confined masonry buildings. *Journal of Building Engineering.* https://doi.org/10.1016/j.jobe.2019.100834
El-Diasity, M., Okail, H., Kamal, O., & Said, M. (2015). Structural performance of confined masonry walls retrofitted using ferrocement and GFRP under in-plane cyclic loading. *Engineering Structures, 94*, 54–69.
ElGawady, M. A., Lestuzzi, P., & Bandoux, M. (2005). In-plane seismic response of URM walls upgraded with FRP. *Journal of Composites for Construction, 2005*, 524–535.
El-Salakawy, T., & Hamdy, G. (2021). Experimental and numerical investigation of strengthening of openings in masonry walls using steel bars and steel wire mesh. *European Journal of Environmental and Civil Engineering.* https://doi.org/10.1080/19648189.2021.1997828
European Committee for Standardisation. (1995). EC6, design of masonry structures. Part 1–1: General rules for buildings—Rules for reinforced and un-reinforced masonry, ENV1996 1–1: Bruxels: CEN.
Flores L.E., & Alcocer S.M. (1996). Calculated response of confined masonry structures. 11th World Conference on Earthquake Engineering, Mexico, paper No. 1830.
Flores, L.E., Mendoza, J.A., & Reyes. C. (2004). Ensaye de mures de mamposterfa con y sin refuerzo alrededer de la abortun. 14th National Congress on Structure Engineering, Mexico; 2004.
Garcí, A. B., et al. (2019). Diagonal compression tests on masonry wallets coated with mortars reinforced with glass fibers. *Materials and Structures.* https://doi.org/10.1617/s11527-019-1360-y
Gostic, S., & Zarnic, R. (1999). Cyclic lateral response of masonry infilled RC frames and confined masonry walls. Proceedings of the 8th North American Masonry Conference, Austin, 3–6 June 1999, 477–488.
Gupta, A., & Singhal, V. (2020). Strengthening of confined masonry structures for in-plane loads: A review. *International Conference on Materials, Mechanics and Structures.* https://doi.org/10.1088/1757-899X/936/1/012031
Hose, Y., & Seible, F. (1999). Performance evaluation database for concrete bridge components, and systems under simulated seismic loads. PEER report 1999/11, Pacific Earthquake Engineering Research Center College of Engineering, University of California, Berkley, U.S.A.
Ishibashi, K., Meli, R., Alcocer, S.M., Leon, F., & Sanchez, T.A. (1992). Experimental study on earthquake-resistant design of confined masonry structure. Proceedings of the tenth world conference on earthquake engineering, Madrid, Spain, 3469–3474.
Kaushik, H. B., Rai, D. C., & Jain, S. K. (2007). Stress–strain characteristics of clay brick masonry under uniaxial compression. *Journal of Materials in Civil Engineering, 19*(9, ASCE), 728–739.
Kuroki, M., Kikuchi, K., Nonaka, H., & Shimosako, M. (2012). Experimental study on reinforcing methods using extra RC elements for confined masonry walls with openings. 15th World Conference on Earthquake Engineering 2012. Lisbona, Portugal.
Lourenco, P. B. (2002). Computations on historic masonry structures. *Progress in Structural Engineering and Materials, 4*(3), 301–319.
Lourenço, P. B., Milani, G., Tralli, A., & Zucchini, A. (2007). Analysis of masonry structures: Review of and recent trends of homogenization techniques. *Canadian Journal of Civil Engineering, 34*, 1443–1457.
Milani, G. (2011). Simple homogenization model for the non-linear analysis of in-plane loaded masonry walls. *Computers & Structures, 89*, 1586–1601.
Page, A. W. (1978). Finite element model for masonry. *Journal of the Structural Division, ASCE, 104*(8), 1267–1285.

El-Diasity *et al. Int J Concr Struct Mater*   (2023) 17:70

Page 30 of 30

Perez, G. et al. (2009). Testing of masonry walls with different lengths: Kinematics and lateral stiffness. XVII National Conference on Earthquake Engineering, Puebla, Mexico.

RILEM TC: 76-LUM. (1994). Diagonal tensile strength tests of small wall specimens. In RILEM (International Union of Laboratories and Experts in Construction Materials), Recommendations for the testing and use of constructions materials, London: E&FN SPON, p. 488–89.

Roca, P., Cervera, M., Gariup, G., & Pelà, L. (2010). Structural analysis of masonry historical constructions, classical and advanced approaches. *Archives of Computational Methods in Engineering., 17*(3), 299–325.

Roca, P., Cervera, M., Pelà, L., Clemente, R., & Chiumenti, M. (2013). Continuum FE models for the analysis of Mallorca Cathedral. *Engineering Structures, 46*, 653–670.

Sandeep, M.V., Renukadevi, S.M., & Somanath. (2013). Influence of reinforcement on the behavior of hollow concrete blocks masonry prism under compression—an experimental and analytical approach. *International Journal of Research in Engineering and Technology*, 106–110.

Shanour, A. S., Mahmoud, A. A., Adam, M. A., & Said, M. (2014). Experimental investigation of concrete beams reinforced with GFRP bars. *International Journal of Civil Engineering and Technology, 5*(11), 154–164.

Singhal, V., & Rai, D. C. (2018). Behaviour of confined masonry walls with openings under in-plane and out-of-plane loads. *Earth Spectra, 34*(2), 807–841.

Tarek, S. S., et al. (2020). Experimental and numerical study of bond between masonry and near-surface mounted steel bars. *Case Studies in Construction Materials*. https://doi.org/10.1016/j.cscm.2020.e00468

Tomazevic, M., & Klemence, I. (1997). Verification of seismic resistance of confined masonry buildings. *Earthquake Engineering and Structural Dynamics, 26*, 1073–1088.

Willam, K.J., & Warnke, E.D. (1975). Constitutive model for the triaxial behavior of concrete. In: Proceedings of International Association for Bridge and Structural Engineering: Seminar on Concrete Structures Subjected to Triaxial Stress, ISMES, Bergamo, Italy, p. 174186.

Yacila, J., Camata, G., Salsavilca, J., & Tarque, N. (2019). Pushover analysis of confined masonry walls using a 3D macro-modelling approach. *Engineering Structures, 201*, 109731.

Yan, H., Minghui, K., & Zifa, W. (2011). Nonlinear analysis for monotonic and low cyclic loading. *Applied Mechanics and Materials, 94–96*, 406–415.

Yanez, F., Astroza, M., Holmberg, A., & Ogaz, O. (2004). Behavior of confined masonry shear walls with large openings. 13th world conference on earthquake engineering, Vancouver, B.C., Canada, No. 343.

Yoshimura, K., Kikuchi, K., Kuroki, M., Nonaka, H., Tae Kim, K., Wangdi, R., & Oshikata, A. (2004). Experimental study on effect of height of lateral forces, column reinforcement and wall reinforcement on seismic behavior of confined masonry walls. 13th World Conference on Earthquake Engineering, Vancouver, Canada, No. 1597.

Yu, P., Silva P., & Nanni, A. (2007). In-plane response of URM walls strengthened with GFRP grid reinforced polyurea. 10th North American Masonry Conference, USA, pp 466–477.

Publisher's Note

Springer Nature remains neutral with regard to jurisdictional claims in published maps and institutional affiliations.

Mosaad El-Diasity   is an Assistant Professor, Structural Engineering Department, Shoubra Faculty of Engineering, Benha University, Egypt.

H. Sayed Salah   is an Assistant lecturer, Structural Engineering Department, Shoubra Faculty of Engineering, Benha University, Egypt.

Mohamed O.R. El-Hariri   is a Professor, Structural Engineering Department, Shoubra Faculty of Engineering, Benha University, Egypt.

Amr A. Gamal   is a Professor, Structural Engineering Department, Shoubra Faculty of Engineering, Benha University, Egypt.

Tarik S. Elsalakawy   is an Associate Professor, Structural Engineering Department, Shoubra Faculty of Engineering, Benha University, Egypt.